**TITLE:** TgLaforin, a glucan phosphatase, reveals the dynamic role of storage polysaccharides in *Toxoplasma gondii* tachyzoites and bradyzoites

**AUTHORS:** Robert D. Murphy[1,2], Cortni A. Troublefield[1a#], Joy S. Miracle[1#], Lyndsay E.A. Young[2], Corey O. Brizzee[2b], Animesh Dhara[1], Ramon C. Sun[2cd], Craig W. Vander Kooi[2cd], Matthew S. Gentry[2cd], Anthony P. Sinai[2*]

1. Department of Microbiology, Immunology, and Molecular Genetics, College of Medicine, University of Kentucky
2. Department of Molecular and Cellular Biochemistry, College of Medicine, University of Kentucky

Current affiliations:

a. Good Samaritan Hospital and Albert B. Chandler Medical Center Emergency Departments, University of Kentucky
b. Demeetra AgBio, 2277 Thunderstick Dr., Lexington, KY, USA
c. Department of Biochemistry and Molecular Biology, College of Medicine, University of Florida, Gainesville, FL, USA
d. Center for Advanced Spatial Biomolecule Research, University of Florida, Gainesville, FL, USA

#These authors contributed equally to this work.

*For correspondence: Anthony P. Sinai, sinai@uky.edu

***Running title:*** TgLaforin regulation of amylopectin granules in Toxoplasma

***Keywords:*** *Toxoplasma gondii* , amylopectin granule, glucan, reversible phosphorylation, laforin, phosphatase, starch, glycogen, steady-state metabolomics, glutamine

**ABSTRACT**

The asexual stages of *Toxoplasma gondii* are defined by the rapidly growing tachyzoite during the acute infection and by the slow growing bradyzoite housed within tissue cysts during the chronic infection. These stages represent unique physiological states, each with distinct glucans reflecting differing metabolic needs. A defining feature of *T. gondii* bradyzoites is the presence of insoluble storage glucans known as amylopectin granules (AGs) that are believed to play a role in reactivation, but their functions during the chronic infection remain largely unexplored. More recently, the presence of storage glucans has been recognized in tachyzoites where their precise function and architecture have yet to be fully defined. Importantly, the *T. gondii* genome encodes activities needed for glucan turnover: a glucan phosphatase (TgLaforin; TGME49_205290) and a glucan kinase (TgGWD; TGME49_214260) that catalyze a cycle of reversible glucan phosphorylation required for glucan degradation by amylases. The expression of these enzymes in tachyzoites supports the existence of a storage glucan, evidence that is corroborated by specific labeling with the anti-glycogen antibody IV58B6. Disruption of reversible glucan phosphorylation via a CRISPR/Cas9 knockout (KO) of TgLaforin revealed no growth defects under nutrient-replete conditions in tachyzoites. However, the growth of TgLaforin-KO tachyzoites was severely stunted when starved of glutamine, even under glucose replete conditions. The loss of TgLaforin also resulted in the attenuation of acute virulence in mice accompanied by a lower cyst burden. Defective cyst formation due to profound changes in AG morphology was also observed in TgLaforin-KO parasites, both *in vitro* and *in vivo*. Together, these data demonstrate the importance of glucan turnover across the *T. gondii* asexual cycle. These findings, alongside our previously identified class of small molecules that inhibit TgLaforin, implicate reversible glucan phosphorylation as a legitimate target for the development of new drugs against chronic *T. gondii* infections.

49 **INTRODUCTION**

50 *Toxoplasma gondii* is an opportunistic protozoan parasite of all warm-blooded animals that
51 infects one-third of humans worldwide (1). Humans are primarily infected through the
52 consumption of an encysted form of the parasite: either the oocysts shed in cat feces or tissue
53 cysts found in undercooked meat from a chronically infected animal (2). Encysted parasites
54 convert into tachyzoites that rapidly divide and disseminate throughout the body of the host,
55 defining the acute phase of infection (3). Under host immune pressure, tachyzoites convert
56 into slow-growing bradyzoites that populate tissue cysts which are found predominantly in the
57 central nervous system and muscle, defining the chronic phase of infection (4). Tissue cysts
58 are believed to persist for the lifetime of the host and possess the ability to reactivate into
59 tachyzoites in the context of immunosuppression. Reactivation can result in the life-threatening
60 symptoms of toxoplasmosis, with toxoplasmic encephalitis being the primary condition leading
61 to mortality (5). The current lack of insights into bradyzoite physiology *in vivo* precludes the
62 basic understanding needed for the development of drugs that either can clear tissue cysts or
63 prevent reactivation (6).

64

65 Until recently, bradyzoites within tissue cysts were considered to be dormant, metabolically
66 inert entities. This view was challenged by our demonstration that encysted bradyzoites
67 replicate (7). Moreover, bradyzoite physiology is both diverse and complex as viewed through
68 the lens of mitochondrial activity, replication status, and, importantly, amylopectin granule (AG)
69 accumulation (8). Although the function of AGs in bradyzoites has not been confirmed, an
70 understanding of the roles of polysaccharides elsewhere suggests that AGs are a source of
71 energy and biosynthetic potential needed for persistence, replication, reactivation, and

72 transmission (9). These assumptions remain to be tested, and thus much like bradyzoites
73 themselves, the role of AGs in the *T. gondii* lifecycle is poorly understood.
74
75 AGs are large glucans found in the cytoplasm of bradyzoites that have classically served as a
76 morphological feature distinguishing them from tachyzoites (10, 11). Early studies
77 characterized AGs as pure amylopectin (12), so AGs are much like plant starch in that they
78 are water-insoluble storage polysaccharides composed of branched chains of glucose. Unlike
79 plant starch, however, AGs contain no detectable amylose (unbranched chains of glucose)
80 (12, 13). More recently, the presence of small, punctate, cytoplasmic glucans in tachyzoites
81 that are only visible by periodic acid-Schiff (PAS) staining have been recognized (14-16), and
82 the presence of the glucan is dependent on the *T. gondii* starch synthase (TgSS;
83 TGME49_222800) (17). Like animal glycogen, this tachyzoite storage polysaccharide is rapidly
84 turned over (14), as has been observed in other protozoa (18-20), and provides glucose for
85 glycolysis (17). The observation that large, insoluble glucans do not accumulate within
86 tachyzoites as they do within bradyzoites suggests that the tachyzoite glucan could be a
87 distinct and labile form of stored glucose, likely glycogen-like, although its exact chemical and
88 structural identity remain unknown.
89
90 Glucose release from starch in plants requires a cycle of direct, reversible glucan
91 phosphorylation to solubilize the starch surface, allowing access to degradation enzymes such
92 as amylases, branching enzymes, and a phosphorylase (21-23). The cycle begins with the
93 addition of phosphate directly to glucose by the glucan, water-dikinase (GWD) and phospho-
94 glucan, water dikinase (PWD) that results in the unwinding of glucose chains within starch,
95 solubilizing the starch surface (24, 25). Glucose-releasing enzymes (amylases) then degrade

96 starch until the glucan-bound phosphate becomes a steric hindrance, at which point a glucan
97 phosphatase is needed to remove the phosphate and reset the cycle (26-29). *T. gondii*
98 encodes all the activities needed for glucan degradation and reversible glucan phosphorylation
99 including the glucan phosphatase, TgLaforin (TGME49_205290) (30), and glucan dikinase, *T.*
100 *gondii* GWD (TgGWD; TGME49_214260) (31, 32) .
101
102 The central role of reversible glucan phosphorylation in plants is seen in *Arabidopsis thaliana*
103 where loss of the plant glucan phosphatase, starch-excess 4 (SEX4), results in excess starch
104 accumulation, aberrant starch morphology, and severely stunted plant growth (33, 34).
105 Additionally, loss of the glucan phosphatase, laforin, in humans results in hyperphosphorylated
106 glycogen that aggregates in neurons and astrocytes causing a fatal, neurodegenerative
107 childhood dementia and epilepsy (35-38). In *T. gondii* , perturbations of several genes related
108 to glucan metabolism also result in a variety of similar defects including aberrant glucan
109 accumulation, rewiring of central carbon metabolism, and virulence defects in mice,
110 highlighting the central metabolic role of glucan metabolism in *T. gondii* (14-17, 39-42).
111
112 In this study, we build on our understanding of reversible glucan phosphorylation and its
113 relevance to parasite metabolism in *T. gondii* . We have recently demonstrated that TgLaforin
114 is the glucan phosphatase in *T. gondii* , and that TgLaforin represents a unique and viable drug
115 target (30, 43, 44). Here, we investigate the role of TgLaforin throughout the asexual stages
116 by knocking out TgLaforin in Type II ME49 parasites. While we expected to observe effects
117 related to the loss of TgLaforin exclusively in bradyzoites where AGs are typically observed,
118 the loss of TgLaforin also resulted in striking phenotypic effects in tachyzoites in a context-
119 specific manner. We thus established a role for TgLaforin, and by extension reversible glucan

120 phosphorylation, across both tachyzoite and bradyzoite life stages. These findings build upon
121 previous studies that increasingly demonstrate a central role for glucan metabolism throughout
122 the parasite's asexual life cycle.
123
124 **RESULTS**
125 ***T. gondii tachyzoites contain a punctate, cytoplasmic glucan***
126 Previous studies have presented biochemical evidence for rapid glucan turnover in *T. gondii*
127 Type I RH tachyzoites (14). Moreover, small granules that stain with PAS have also been noted
128 in the cytoplasm of tachyzoites (14, 16, 17). Under acid-stress conditions, these tachyzoite
129 glucans have been biochemically characterized as pure amylopectin, and resemble AGs seen
130 in bradyzoites (13). To further characterize the nature of this tachyzoite glucan, we used
131 multiple methods to visualize them under unstressed, normal growth conditions (**Figure 1A**).
132 PAS staining confirmed that Type II ME49 tachyzoites contain small punctate granules
133 distributed throughout the cytoplasm. To determine if these PAS-stained granules in
134 unstressed tachyzoites were more glycogen- or starch-like, they were stained with IV58B6.
135 IV58B6 is an anti-glycogen IgM monoclonal antibody that has previously been demonstrated
136 to be specific to glycogen (45, 46) by recognizing the highly frequent branch-points found in
137 glycogen (47). Moreover, IV58B6 does not detect other glucans such as amylopectin or
138 amylose (the primary constituents of plant starch) (48). Tachyzoites stained with IV58B6 in a
139 similar pattern to PAS-stained parasites, containing small punctate granules distributed
140 throughout the cytoplasm (**Figure 1A**), suggesting that the glucan found in tachyzoites is more
141 glycogen-like than starch-like. Finally, as is well-known, *T. gondii* tachyzoites contain almost
142 no visible glucan within their cytoplasm when visualized by transmission electron microscopy
143 (TEM) (**Figure 1A**), suggesting that the glucan detected by both PAS staining and IV58B6 is

144 either water-soluble or too small to be visualized, consistent with this glucan being glycogen-
145 like.
146 In contrast, bradyzoites have been extensively characterized as containing starch-like AGs
147 (11-13, 49). After *in vitro* bradyzoite conversion, much of the cytoplasm stained heavily with
148 PAS (**Figure 1A**). Interestingly, IV58B6 staining intensity appeared to correlate negatively with
149 *Dolichos biflorus* agglutinin (DBA) staining intensity that defines the cyst wall, implying that
150 IV58B6 does not stain the PAS-stained glucan in mature bradyzoites, further reinforcing the
151 observation that structurally distinct polysaccharides exist in tachyzoites and bradyzoites
152 (**Figure 1A**). Finally, unlike in tachyzoites, AGs were readily identified as electron-lucent
153 structures throughout the bradyzoite cytoplasm by TEM (**Figure 1A**).
154 To verify the specificity of PAS and IV58B6 for glucose polymers, tachyzoites and bradyzoites
155 were treated with acid-$\alpha$-amyloglucosidase (GAA) after parasite fixation and before staining.
156 GAA cleaves both $\alpha$-1,4- and $\alpha$-1,6-glycosidic bonds and can therefore completely digest
157 glucans into glucose monomers. Indeed, GAA treatment resulted in the disappearance of
158 staining with both reagents (**Figure 1B**) demonstrating their specificity for glucose polymers.
159
160 ***TgLaforin colocalizes with the tachyzoite glucan***
161 Because *T. gondii* encodes TgLaforin, a glucan phosphatase that is more animal-like than
162 plant-like (43, 44), we reasoned that TgLaforin could be involved in the metabolism of the
163 glycogen-like glucan found in tachyzoites. To determine if TgLaforin co-localizes with the
164 tachyzoite glucan, endogenous TgLaforin was epitope-tagged with hemagglutinin (HA) in *T.*
165 *gondii* Type II ME49ΔHXGPRT parasites with a CRISPR/Cas9 mediated strategy (**Figure 2A**)
166 (50). Successful tagging of TgLaforin was confirmed by western blotting (**Figure 2B**).
167 Immunofluorescence analysis (IFA) of *T. gondii* tachyzoites indicated that TgLaforin is present

168 in small puncta throughout the cytoplasm, similar to the distribution of the tachyzoite glucan
169 (**Figure 2C**). Surprisingly, TgLaforin was not detected in *in vitro* bradyzoites by IFA, 6 days
170 post conversion.
171 To verify that TgLaforin levels decrease during the tachyzoite to bradyzoite transition, we
172 converted *T. gondii* tachyzoites to bradyzoites in cell culture using alkaline stress for 6 days
173 and then probed the converted parasites using western blot analysis. As observed using IFA,
174 TgLaforin-HA expression decreased dramatically over the course of bradyzoite differentiation
175 (**Figure 2D**). Transcriptomic data from a previous study obtained from ToxoDB.org indicates
176 that the transcript levels for TgLaforin do not substantially change over the course of
177 differentiation, suggesting the possibility that levels of TgLaforin protein are regulated by post-
178 translational mechanisms (51).
179 To determine if TgLaforin colocalizes with the glucan present in tachyzoites, we co-stained
180 TgLaforin-HA tachyzoites with either PAS or IV58B6 along with an anti-HA antibody. In
181 tachyzoites, TgLaforin colocalized with both PAS (**Figure 2E**) and with IV58B6 (**Figure 2F**),
182 suggesting its involvement in the metabolism of the tachyzoite glucan.
183
184 ***Initial characterization of TgLaforin-KO tachyzoites***
185 To dissect the role of TgLaforin in *T. gondii* glucan metabolism, TgLaforin was knocked out
186 using CRISPR/Cas9 to disrupt the gene with a pyrimethamine-resistant form of the
187 dihydrofolate reductase (DHFR-TS*) under a *Neospora caninum* GRA7 (NcGRA7) promoter
188 (52, 53) (**Figure 3A**). In agreement with a genome-wide CRISPR KO screen (54), TgLaforin is
189 a non-essential gene under standard cell culture conditions, as multiple TgLaforin-KO clones
190 were successfully recovered. Integration of the DHFR-TS* construct into the TgLaforin locus
191 was verified using inside/out PCR at the chimeric locus and by verifying the loss of TgLaforin

192 transcription (**Figures 3B, C**). The TgLaforin-KO line further used in this study (designated
193 "ΔTgLaf") was complemented by the introduction of an epitope tagged gene driven by the
194 TgLaforin promoter. The complementation construct was introduced at an ectopic site in the
195 genome that lacks known coding sequences or regulatory elements on chromosome VI
196 (**Figure S1A**), while leaving the ΔTgLaf/DHFR-TS* KO lesion intact for true complementation
197 (55). This complemented strain, henceforth designated "COMP," was successfully isolated and
198 confirmed by PCR (**Figure S1B**). Expression levels and localization were similar to those seen
199 in the TgLaforin-HA line as confirmed by western blotting and IFA (**Figures S1C-D**),
200 To evaluate effects of a TgLaforin-KO, glucan levels in WT and ΔTgLaf tachyzoites were first
201 compared using our suite of glucan detection techniques (**Figure 3D**). Surprisingly, the size
202 and number of PAS-stained granules were not significantly changed in ΔTgLaf tachyzoites
203 relative to WT parasites. Levels of IV58B6 also remained unaltered after the loss of TgLaforin,
204 and no aberrant glucan accumulation was observed by TEM as has been previously reported
205 when genes related to AG or central carbon metabolism were knocked out in *T. gondii*
206 tachyzoites (**Figure 3D**) (14, 39, 41, 42, 56, 57). Loss of glucan phosphatases in plants and
207 animals results in aberrant glucan accumulation, and such a phenotype was not observed
208 here.

209 ***Loss of TgLaforin results in upregulation of glutaminolysis and glutamine dependence***
210 ***in tachyzoites***

211 Glucan catabolism is significantly affected by the presence of covalently bound phosphate,
212 and, therefore, loss of glucan phosphatases has profound downstream metabolic impacts in
213 other systems (58, 59). We thus speculated that loss of TgLaforin would result in the reduced
214 efficiency of glucan utilization in tachyzoites and also affect downstream central carbon
215 metabolism. To test this hypothesis, we used gas chromatography/mass spectrometry

216 (GC/MS) steady-state metabolomic analysis of 3 μm filter-purified, syringed-passaged
217 intracellular tachyzoites employing a previously developed sample preparation technique (60).
218 Previously, it was demonstrated that *T. gondii* tachyzoites primarily utilize glucose and
219 glutamine to drive central carbon metabolism, synthesize macromolecules, and proceed
220 normally through the lytic cycle (61). Glucose primarily fuels glycolysis, and glutamine
221 undergoes glutaminolysis to drive the tricarboxylic acid (TCA) cycle. In the absence of glucose,
222 *T. gondii* can upregulate both glutaminolysis and gluconeogenesis to make up for the loss of
223 glucose (61, 62).
224 While ΔTgLaf metabolite levels remained unaltered relative to WT tachyzoites across much of
225 the TCA cycle, steady-state levels of metabolites immediately downstream of glutamine were
226 consistently more abundant in ΔTgLaf parasites compared to their WT counterparts (**Figure**
227 **4A**), supporting our hypothesis that ΔTgLaf parasites were deficient in glucan/glucose
228 utilization. An increase in metabolites downstream of glutamine in ΔTgLaf parasites
229 demonstrates that ΔTgLaf parasites are possibly compensating for deficiencies in glucose
230 metabolism, supporting a role for the tachyzoite glucan in intermediate *T. gondii* glucose
231 metabolism.
232 To determine if loss of TgLaforin resulted in increased dependence on glutamine due to
233 impaired access to glucose, we performed plaque assays in the presence and absence of
234 glutamine (**Figure 4B**). In replete media, ΔTgLaf parasites established a similar number of
235 plaques, indicating no defect in infectivity, that were slightly larger than both the WT and COMP
236 lines after 10 days of growth (**Figure 4C**). To test the effects of glutamine starvation on ΔTgLaf
237 parasites, glutamine was removed from plaque assays after parasite invasion to evaluate the
238 effects of glutamine removal on parasite growth independent of the initial invasion event. In
239 the absence of glutamine, ΔTgLaf parasites were unable to form visible plaques, whereas both

240 the WT and COMP parasites formed plaques comparable to those formed under glutamine-
241 replete conditions (**Figures 4B, C**).

242 ***TgLaforin is required for repeated rounds of progression through the lytic cycle***

243 To determine which aspects of the *T. gondii* lytic cycle were impaired in the absence of
244 glutamine, preventing visible plaque formation in ΔTgLaf parasites, the effects of glutamine
245 starvation on initial parasite replication and egress (stimulated with both A23187 and zaprinast)
246 were evaluated (63, 64). In both assays, intracellular parasites were pre-starved of glutamine
247 for at least 72 h before assay initiation. Surprisingly, glutamine starvation had no effect on
248 stimulated egress or initial parasite replication across the three lines (**Figures S2A-C**). These
249 data demonstrate that the absence of plaques under glutamine deficient conditions cannot be
250 pinpointed to a single aspect of the ΔTgLaf lytic cycle, and that the reason for the apparent
251 absence of plaques manifested later in the infection cycle.

252 Plaques develop due to repeated cycles of lysis resulting in the clearance of infected cells over
253 time. The absence of visible clearance prompted us to examine infected host-cell monolayers
254 for clusters of infected cells using a higher magnification than is typically used in a traditional
255 plaque assay. Low numbers of parasites were seeded onto glass coverslips and fixed at 3-
256 and 6-days post-infection, allowing for visualization of developing plaques at a high
257 magnification. In these experiments, glutamine-depleted host cells were pre-starved of
258 glutamine prior to infection with parasites to allow for potential for invasion defects. Importantly,
259 ΔTgLaf parasites demonstrated similar infectivity to WT parasites under both glutamine-replate
260 and depleted conditions, indicting no gross initial invasion defect.

261 After 3 days of growth, no statistical differences of nascent plaque sizes were noted between
262 glutamine-replete and starved conditions in both the WT and COMP lines. However, ΔTgLaf
263 parasites in glutamine starved conditions were already 1.5x smaller in area than their

264 counterparts in replete conditions (**Figure 4D**). By day 6 of growth, this difference had widened
265 to a >3x difference between glutamine replete/depleted ΔTgLaf parasites (**Figure 4E**). Such a
266 difference was not detected between the two conditions in WT/COMP parasite lines. By
267 measuring the internal clearing area relative to the total plaque perimeter, it was also noted
268 that ΔTgLaf parasites were much less capable of forming clearings than the WT/COMP lines
269 (**Figures S2D, E**), rather they formed clusters of infected cells akin to "turbid plaques" due to
270 their presumed inability to compete with host cell growth, as the infection progressed. This
271 observation explains the apparent absence of plaques seen at the lower magnification used in
272 traditional plaque assays (**Figure 4B**). The modified plaque assay therefore confirmed that the
273 loss of TgLaforin penalized the summation of repeated rounds of the energy-demanding lytic
274 cycle rather than one particular aspect of the lytic cycle. Representative images from this assay
275 can be found in **Figure S2D**.
276
277 ***Loss of TgLaforin results in aberrant bradyzoite AGs in vitro***
278 To determine if loss of TgLaforin resulted in bradyzoite conversion defects or aberrant AG
279 accumulation, parasites were converted to bradyzoites *in vitro* using alkaline stress. During
280 differentiation, the parasitophorous vacuole membrane (PVM), delimiting the replicative niche
281 established by tachyzoites, converts into the cyst wall that surrounds bradyzoites within their
282 host cell (65, 66). The cyst wall is heavily glycosylated and contains N-acetylgalactosamine
283 (Gal-NAc) that is detectible with DBA (67). Using DBA intensity as a marker for differentiation
284 progress, no penalty was imposed by the loss of TgLaforin on cyst wall formation over the
285 course of six days, indicating that ΔTgLaf parasites are not defective in this aspect of
286 bradyzoite differentiation (**Figure 5A**). Somewhat surprisingly, ΔTgLaf mutant parasites tended
287 to exhibit stronger labeling with DBA at day 6. We additionally assessed the levels of

288 accumulated glucans using PAS staining (**Figure 5B**). Semi-quantitative analysis of PAS
289 intensity within vacuoles during stage conversion showed an expected increase over time, but
290 no significant difference between the WT and ΔTgLaf parasites was detected over the time
291 course examined.
292 Because PAS is not specific to glucans and can stain other glucose-containing molecules such
293 as glycosylated protein and provides no resolution on glucan morphology, we utilized TEM to
294 gain higher resolution on AG formation during bradyzoite differentiation. After 6 days of
295 conversion, WT parasites produced AGs that were circular/ovoid and white (**Figure 5C**). In
296 contrast, ΔTgLaf parasites contained irregular AGs that were morphologically distinct from AGs
297 that were observed in WT parasites. AGs in ΔTgLaf parasites appeared amorphous and
298 grayer, while appearing to occupy more area of the parasite cytoplasm compared to WT
299 parasites. To quantify this phenotype, the area of AGs was calculated relative to total parasite
300 area to determine the percentage of the parasite body occupied by AGs in both WT and ΔTgLaf
301 strains (**Figure 5D**). Strikingly, AGs occupied approximately 4x more relative area in ΔTgLaf
302 parasites when compared to WT, indicating that PAS staining may lack the specificity to
303 capture this difference. When analyzed on an 8-bit gray scale, AGs in ΔTgLaf parasites were
304 significantly grayer than those found in WT parasites, highlighting potential chemical
305 differences (such as hyperphosphorylation) resulted in differential interactions of ΔTgLaf AGs
306 with the TEM contrast reagents, likely the heavy metals used in processing (**Figure 5E**).
307 Examination and quantification of AGs in the COMP line revealed that complementation of
308 TgLaforin restored most of the circular/ovoid AGs while they also occupied less space in the
309 cytoplasm and were overall more like those found in WT parasites (**Figures 5C-E**). Thus, cell
310 culture experiments demonstrate that the loss of TgLaforin presents itself in both a context and
311 stage-specific manner.

312 ***Loss of TgLaforin results in attenuated virulence and cyst formation in vivo***

313 We hypothesized that loss of TgLaforin may impose a steep penalty under the stresses and
314 potential nutrient scarcities encountered *in vivo* as it does when nutrients (such as glutamine)
315 are scarce *in vitro*. To test this hypothesis, equal numbers of male and female CBA/J mice
316 were infected with 100 tachyzoites intraperitoneally (i.p.) and monitored daily using a
317 previously developed five-stage body index score to track the severity of symptoms associated
318 with a tachyzoite infection over the course of 28 days (68).

319 Mice infected with WT parasites began demonstrating symptoms of infection ten days after
320 infection with tachyzoites (**Figure 6A**). However, mice infected with ΔTgLaf parasites did not
321 begin to exhibit symptoms until 15 days after infection. Moreover, mice that became
322 symptomatic from WT parasite infections often proceeded through all stages of symptomology,
323 and only a minor proportion of mice that became sick were able to recover from infection (>70%
324 of mice became moribund or died). Infection from ΔTgLaf parasites, however, resulted in the
325 majority of mice only developing mild symptoms (Stage 2 or less) with many of these mice
326 recovering (**Figure 6A**). The attenuated capacity of the ΔTgLaf parasites to cause symptoms
327 in mice was reflected in the mortality rates of the infected mice: infection with WT parasites
328 resulted in 73% mortality rate after 28 days whereas ΔTgLaf parasites only caused 17%
329 mortality (**Figure 6B**). Complementation of TgLaforin partially rescued this defect in virulence
330 as COMP parasites resulted in an earlier onset of symptomatic infection at Day 11, and the
331 majority (53%) of mice succumbed to infection during the first 28 days (**Figures 6A, B**).

332 Because the acute phase of infection was significantly attenuated by the loss of TgLaforin, we
333 hypothesized that cyst numbers would be significantly lowered. To determine the number of
334 cysts formed after 28 days of acute infection, we used a previously established protocol for
335 harvesting and counting tissue cysts from infected mouse brains, following purification on

336 Percoll gradients (7, 69). Consistent with the ability of ΔTgLaf parasites to stage convert in
337 culture, mutant parasites were able to establish tissue cysts *in vivo*. However, the number of
338 cysts recovered from ΔTgLaf infected animals was lower than those obtained from WT infected
339 animals (**Figure 6C**). Restoration of TgLaforin in the COMP line effectively restored tissue cyst
340 yields.
341
342 ***ΔTgLaf tissue cysts can reestablish infections in naïve mice***
343 To determine if the loss of TgLaforin impacted the overall viability/infectivity of *in vivo* tissue
344 cysts, we examined the disease progression in WT, ΔTgLaf, and COMP infected animals
345 following injection of 20 tissue cysts i.p. Consistent with prior data, infection with tissue cysts
346 results in markedly lower pathology and consequent mortality during the acute phase for WT
347 as well as both the ΔTgLaf and COMP lines (**Figure 7A, B**) (68). The death rate from cyst
348 infection did not differ statistically among the three lines. Twenty-eight days post-infection, cyst
349 burdens were again enumerated for each line. ΔTgLaf parasites were once again much less
350 competent at forming cysts *in vivo*. However, unlike the tachyzoite infection, the COMP line
351 was unable to rescue this defect in cyst formation (**Figure 7C**), suggesting that physiological
352 and metabolic changes associated with the loss of TgLaforin manifest differently based on the
353 life cycle stage, impacting their capacity to be complemented.
354
355 ***Proper cyst formation relies on the presence of TgLaforin***
356 Recent work has also demonstrated that loss of phosphoglucomutase 1, an enzyme related to
357 AG metabolism, results in smaller cysts (70). Our prior work established that bradyzoite
358 replication within tissue cysts occurs in a cyclical pattern that is reflected in the packing density
359 of bradyzoites within the cyst (7). Notably, expansion of tissue cyst diameter precedes

360 replication. We therefore analyzed the packing densities and diameters of cysts from WT,
361 ΔTgLaf, and COMP lines to investigate the relationship between the number of bradyzoites
362 within a cyst to the overall volume of the cyst.
363 Packing density is calculated by dividing the number of bradyzoite nuclei within an optical
364 section of a cyst by the volume of the cylinder representing that optical section (7). ΔTgLaf
365 parasites had significantly lower packing density than WT or COMP parasites at both 4 and 6
366 weeks post-infection (**Figure 8A,C** and **Figure S3A,B**). This indicates that loss of TgLaforin
367 resulted either in lower replication within the cyst, increased parasite death, or both. These
368 data provide the first evidence of a mutation resulting in lower bradyzoite numbers within tissue
369 cysts as opposed to merely assessing overall cyst numbers.
370 To determine the relationship of packing density to cyst diameter, we analyzed the cyst
371 diameter alone as a surrogate for cyst expansion at both time points (**Figure 8B,D** and **Figure**
372 **S3C,D)**. At 4 weeks post-infection, ΔTgLaf tissue cysts were smaller in diameter than WT and
373 COMP cysts. At week 6, however, there was no difference between average diameter of
374 ΔTgLaf tissue cysts and that of the WT and COMP lines. Together, these data indicate that the
375 decreased packing density seen in ΔTgLaf parasites is a result of continued cyst expansion
376 accompanied by reduced bradyzoite replication, increased bradyzoite death, or a combination
377 of these factors.
378 To establish whether the changes in AG levels and morphology observed in ΔTgLaf
379 bradyzoites following *in vitro* conversion were observed *in vivo* by TEM, we adapted a protocol
380 designed to capture and image low abundance cells by TEM by making it compatible with our
381 tissue cyst purification protocol (see Methods) (71, 72). TEM imaging revealed that while WT
382 parasites formed largely normal/canonical AGs *in vivo* as seen *in vitro* (**Figure 9** [compare with
383 **Figure 5A**]), ΔTgLaf parasites contained almost exclusively aberrant AGs that mirrored the

384 same morphological defects seen *in vitro* (**Figure 9** and **Figure S4**). ΔTgLaf AGs were
385 irregularly sharpened with a flat, multi-lobed appearance. Importantly, COMP parasites neither
386 over-accumulated nor formed aberrant AGs, demonstrating that this defect is specific to loss
387 of TgLaforin (**Figure 9**).
388 In addition to containing aberrant AGs, the internal morphology of ΔTgLaf parasites appeared
389 to be altered by the presence of the AGs, as significant organelle displacement was also noted.
390 Many of the ΔTgLaf parasites also appeared hollow or "ghost-like" in appearance resulting
391 from their unstained/absent cytoplasm, which included the apparent loss of the nucleus in
392 several parasite forms. These data suggest that a significant number of the ΔTgLaf bradyzoites
393 were inviable within the cyst (additional images of parasites from both WT and ΔTgLaf
394 parasites are presented in **Figure S4**) and that increased death is a significant contributing
395 factor to the reduced packing density (**Figure 8**). Together, these direct and selective impacts
396 of TgLaforin's loss on both bradyzoite viability and growth *in vivo* establish TgLaforin as a
397 potentially druggable target.
398

399 **DISCUSSION**

400 The asexual life cycle of *Toxoplasma gondii* is defined by two fundamentally distinct forms: the
401 rapidly replicating tachyzoite and the slowly growing bradyzoite. These forms represent distinct
402 physiological states that can be further subdivided, particularly within encysted bradyzoites
403 (73). Insights into these physiological states, inferred from transcriptomic analyses, are
404 reinforced in emerging metabolomic studies (74, 75). In these studies, glucose and glutamine,
405 which are both linked to energetics, biosynthesis, and intermediary metabolism, appear as
406 critical metabolites. Importantly, glucose can be stored in polymers like glycogen and
407 amylopectin during times of low energy need. Stored glucose can be present in an accessible

408 and labile form for rapid mobilization such as glycogen, or in a less soluble forms as AGs from
409 which it can be accessed more slowly (76). Reversible glucan phosphorylation facilitates the
410 breakdown of such glucan polymers by disrupting the crystalline helices on the glucan surface
411 (77). *T. gondii* encodes the capacity for reversible glucan phosphorylation (30, 32, 43, 44).
412 The contribution of this process to tachyzoite and bradyzoite biology was evaluated through
413 targeted manipulation of the glucan phosphatase, TgLaforin.
414 The accumulation of AGs within bradyzoites and their apparent absence in tachyzoites has
415 been used as discriminator between these life cycle stages. Detailed examination, however,
416 presents a considerably more nuanced picture, alongside emerging evidence that points to
417 rapid glucan turnover within tachyzoites (14). Here, using an IgM monoclonal antibody
418 (IV58B6) that specifically recognizes glycogen-like glucose polymers (45), we demonstrate
419 that the stored glucan within tachyzoites is structurally closer to animal glycogen than the
420 insoluble plant-like AG granules found in bradyzoites (12). This duality between life stages may
421 be additionally reflected in the observation that TgLaforin, the glucan phosphatase, and
422 TgGWD (TGME49_214260), the accompanying kinase that is predicted to phosphorylate *T.*
423 *gondii* glucan polymers, trace their structural lineages to animals and plants, respectively (43,
424 44). The glycogen-like glucan polymer appears to be specific to tachyzoites as its levels
425 decrease upon *in vitro* differentiation while the overall PAS intensity increases (**Figure 1A**).
426 This suggests that the tachyzoite glucan and bradyzoite AG are architecturally distinct
427 polymers with respect to both branching frequency, solubility, and phosphorylation status
428 (**Figure 2D**). The glucose-based nature of both particles is supported by the elimination of both
429 IV58B6 and PAS staining with $\alpha$-amyloglucosidase treatment (**Figure 1B**).
430

431 To address the contribution of stored glucans in both tachyzoites and bradyzoites, we disrupted
432 the glucan phosphatase TgLaforin. This enzyme preferentially removes phosphate groups
433 from the C3 carbon on glucose facilitating access to enzymes that release glucose (30). The
434 loss of other glucan phosphatases such as SEX4 in *A. thaliana* and laforin in mammals is
435 accompanied by excessive accumulation of aberrant starch and hyperphosphorylated
436 glycogen in plants and animals (33, 34, 37, 38, 78). Surprisingly, given these penalties in other
437 systems, ΔTgLaf tachyzoites exhibited no gross morphological changes in glucan content,
438 consistent with a recent study in which TgGWD was knocked out (32). These observations
439 contrasts with other KO studies of glucan pathway associated proteins such as CDPK2,
440 glycogen phosphorylase, the PP2A holoenzyme, and α-amylase which all reported
441 exaggerated glucan accumulation in tachyzoites (14, 39, 41, 42, 56).
442 Despite the absence of glucan accumulation in ΔTgLaf tachyzoites, the loss of this gene exerts
443 an effect on tachyzoite glucan metabolism. Consistent with the metabolic defects associated
444 with the loss of laforin in humans (58), loss of TgLaforin in *T. gondii* resulted in altered central
445 carbon metabolism that manifested as ΔTgLaf parasites' dependence on glutamine. ΔTgLaf
446 tachyzoites' dependence on glutamine supports recent studies demonstrating that tachyzoites
447 utilize storage glucans for glucose allocation (14, 17) because the presumed loss of efficient
448 glucan degradation results in tachyzoite dependence on glutamine (**Figures 4B, C**). As *T.*
449 *gondii* tachyzoites primarily utilize glucose and glutamine to support their rapid growth, this
450 dependence on glutamine reinforces previous observations that glutamine can substitute for
451 glucose in this altered metabolic landscape (61, 79).
452 These results are consistent with many previous studies that disrupt glucose and/or glucan
453 metabolism, but contrast with others. Disruption of TgGT1 (TGME49_214320), the only
454 plasma-membrane glucose transporter in *T. gondii* (61, 80), or TgHK (TGME49_265450), the

455 *T. gondii* hexokinase, resulted in upregulation of gluconeogenesis, and parasite growth was
456 highly attenuated with glutamine depletion (79). Most strikingly, parasites lacking starch
457 synthase (TgSS; TGME49_222800) displayed no dependence on glutamine and, in fact, grew
458 faster than WT parasites when both glucose and glutamine were removed from the culture
459 media (17). Interestingly, however loss of TgSS did result in lower glucose flux through
460 glycolysis, consistent with our findings that demonstrate a role for the tachyzoite glucan in
461 glucose allocation. This finding may suggest that while the absence of AG in the ΔTgSS
462 parasites may not be detrimental, overaccumulation as observed in ΔTgLaf cysts can
463 contribute to toxicity (**Figure 9**). Perturbations of other glycolytic enzymes also demonstrated
464 varied effects related to the presence of glutamine: loss of the glycolytic enzyme
465 glyceraldehyde-3-phospahte dehydrogenase (GAPDH1) could be rescued with high levels of
466 glutamine (81), but glutamine could not rescue pyruvate kinase (TgPYK1) knockdown
467 parasites (57). Our data indicate that loss of access to key nutrients such as glucose and
468 glutamine has a profound impact on the repeated rounds of the lytic cycle without being
469 attributable to one specific process within the cycle, suggesting that the penetrance of the
470 phenotypic defect manifests cumulatively over time, rather than being hard wired in each
471 infection cycle (**Figures 4D, E**).
472 Despite glucan metabolism being historically viewed as being important in the chronic infection,
473 TgLaforin protein expression decreased during the tachyzoite to bradyzoite conversion *in vitro*
474 even though its transcript levels do not change (**Figures 2C, D**). This could be a transient
475 observation as the downregulation of glucan catabolism during conversion would facilitate
476 accumulation of AGs for the chronic infection. We therefore examined how the loss of
477 TgLaforin affected the capacity of ΔTgLaf parasites to differentiate *in vitro*. The ΔTgLaf
478 parasites exhibited no defect in AG-accumulation kinetics, detected by PAS staining, or in cyst

479 wall formation, detected with DBA lectin (**Figure 5A, B**). The lack of difference in PAS labeling
480 between both the WT and the ΔTgLaf lines, however, did not reveal the differences noted by
481 TEM. As initially hypothesized would be the case in both tachyzoites and bradyzoites, loss of
482 TgLaforin resulted in aberrant AG accumulation within *in vitro* bradyzoites that is marked by
483 changes in both level and morphology (**Figures 5C-E**), as seen in plants and vertebrates (33,
484 34, 36-38). AGs in the ΔTgLaf parasites were not only present at higher levels but were
485 potentially chemically distinct considering their differential binding to TEM contrast metals.
486 Given that TgLaforin is a confirmed glucan phosphatase (30), we speculate that AG
487 hyperphosphorylation may account for both altered morphology and appearance by TEM.
488 These context-specific phenotypes suggested that the ΔTgLaf mutant would manifest
489 phenotypic differences in both the acute and chronic phases on infection *in vivo*. Indeed, the
490 loss of TgLaforin was associated with a markedly reduced symptomology and associated
491 mortality compared to both the parental and complemented parasites during acute tachyzoite-
492 initiated infection (**Figures 6A, B**). Not only was there a delay in symptomatic disease, but also
493 a reduction in disease severity and overall cyst burden. Symptomology in the acute infection
494 is driven by an increasing parasite burden driving an overexuberant host inflammatory
495 response. The delayed symptom onset suggests growth inhibition by the stringent *in vivo*
496 environment that more effectively controls ΔTgLaf parasite infection with less robust
497 inflammation. Notably, the delayed and milder course of the tachyzoite infection resulted in a
498 lower overall cyst burden in surviving animals compared to infection with both WT and COMP
499 parasites (**Figure 6C**).
500 Bradyzoite replication within cysts is preceded by the expansion of the cyst to accommodate
501 newly formed parasites (7). Bradyzoite occupancy can be established by quantifying the
502 number of nuclear cross sections in imaged tissue cysts to define the packing density. The

503 finding that ΔTgLaf cysts were smaller, and less densely packed than WT or complemented
504 cysts, indicates that TgLaforin, and by extension reversible glucan phosphorylation, may have
505 a significant impact on the progression of the chronic phase of infection, manifesting at the
506 level of encysted bradyzoites.

507 The capacity of ΔTgLaf cysts to initiate new infections was assessed *in vivo*. Consistent with
508 other studies (7, 68), infection with tissue cysts is associated with limited symptomology and
509 low overall mortality. Similar to what was observed with tachyzoite-initiated infections, the
510 ΔTgLaf parasites consistently presented with lower cyst burdens relative to WT cyst infections.
511 One puzzling outcome, however, is the fact that the complemented line failed to rescue the
512 overall cyst burden for tissue cyst-initiated infections, despite completely rescuing infections
513 initiated with tachyzoites. This recurring theme for the penetrance or lack thereof in a context
514 specific manner appears to apply selectively to the rescue of the phenotype as well.

515 As was observed *in vitro*, TEM revealed a phenotype of aberrant AG accumulation which was
516 accompanied by apparent extensive parasite death **(Figure 9)**. Together, these phenotypes
517 manifest as AGs occupying much of the cytoplasm, the enucleation of parasites, and the
518 detection of "ghost parasites" that appear to be empty shells surrounded by the cytoskeleton.
519 The presence of "ghost parasites" adjacent to seemingly normal parasites highlights the
520 variable penetrance of the phenotype in what is a clonal population, given that each tissue cyst
521 originates from a single parasite. These finding suggest that AG metabolism is under tight
522 control as dysregulated accumulation can result in cumulative defects resulting in toxicity and
523 death. The high frequency of these abnormal parasites suggests that reversible glucan
524 phosphorylation and TgLaforin specifically represent legitimate bradyzoite specific drug
525 targets. We recently described a small molecule that inhibits recombinant TgLaforin (30) which
526 serves as a potential starting point in the development of a new class of anti-*Toxoplasma*

527 therapeutic agents. Particularly exciting in this context is the fact that a class of drugs exhibiting
528 efficacy with tissue cyst clearance (atovaquone (82), endochin-like quinolones (83), and
529 JAG21 (84)) all target mitochondrial respiration. When glucose is limiting, mitochondrial
530 respiration can be driven by glutamine. This provides an opportunity for combination therapy
531 to promote the clearance of toxoplasma tissue cysts as a means of mitigating the risk of
532 reactivation.
533
534 **METHODS**
535 ***Fibroblast and parasite culture and maintenance***
536 All parasite lines were maintained in human foreskin fibroblasts (HFFs; ATCC) in Minimal
537 Essential Media-α (MEM-α; Gibco) supplemented with 7% heat-inactivated fetal bovine serum
538 (FBS; Gemini Bio), 100 U/mL penicillin, 100 μg/mL streptomycin, and an additional 2 mM L-
539 glutamine (Gibco; 4 mM total L-glutamine). Cells and parasites were incubated at 37ºC and
540 5% $CO_2$ in a humidified incubator. Genetically modified parasites were maintained in MEM-α
541 containing 7% dialyzed FBS (Gemini Bio) and either pyrimethamine (1 μM), mycophenolic
542 acid/xanthine (MPA: 25 μg/mL, xanthine: 50 μg/mL), or 6-thioxanthine (6-Tx: 80 μg/mL).
543 Assays analyzing the effects of glutamine deprivation used Dulbecco's Modified Eagle Medium
544 (DMEM). Both glutamine-replete (Gibco, 11966025) and depleted (Gibco, 11054020) DMEM
545 were supplemented with 7% dialyzed FBS. Glutamine-replete media from the supplier lacked
546 other key nutrients and was modified to contain 5 mM glucose, 1 mM sodium pyruvate, and 4
547 mM L-glutamine.
548
549
550

551 ***Generation of T. gondii mutant lines***

552 *Type II ME49ΔHXGPRT* ("WT"—the parental line utilized to generate all other lines in this
553 study): This line was generated in a previous study using CRISPR/Cas9 targeting of
554 TgHXGPRT and selection with 6-Tx (68).

555 *TgLaforin-3xHA-HXGPRT*: TgLaforin was epitope tagged with HA at the C-terminus using
556 CRISPR-Cas9 to disrupt the TgLaforin 3'UTR immediately downstream of the endogenous
557 stop codon as has been previously described (50). Briefly, a sgRNA immediately downstream
558 of the TgLaforin stop codon was designed using the EuPaGDT design tool
559 (http://grna.ctegd.uga.edu). The top hit was selected (**Table S1**) and used to replace the
560 sgRNA sequence in pSAG1::CAS9-U6::sgUPRT, a plasmid containing both Cas9-green
561 fluorescent protein (GFP) and an interchangeable sgRNA scaffold; (**Table S2**) (53).
562 Replacement of the interchangeable sgRNA was accomplished using a Q5 site-directed
563 mutagenesis kit (**Table S3**) (New England BioLabs). The TgLaforin-HA tagging construct was
564 generated by amplifying the 3' end of the TgLaforin-HA construct generated for
565 complementation (see generation of COMP line below and **Tables S2 and S3**) along with the
566 connected HXGPRT selectable marker. Both the TgLaforin-HA PCR-amplicon and the
567 CRISPR-Cas9-GFP were transfected into $1.4 \times 10^7$ *T. gondii* ME49ΔHXGPRT parasites (2:1
568 insert:plasmid molar ratio; 30 μg DNA total) by electroporation with a time constant between
569 0.16 and 0.20 msec (BioRad Gene Pulser II). After 24 h, surviving parasites were syringe-
570 passaged from infected HFFs with a 27 G needle to lyse host cells, and gravity-filtered through
571 a 10 μm filter to remove host-cell debris. Successful transformants were then enriched by use
572 of fluorescence-activated cell sorting (FACS; Sony SY3200, installed in a biosafety level II
573 cabinet) to select parasites expressing Cas9-GFP from the transfected plasmid by isolating
574 GFP+ parasites. HFFs were infected with GFP+ parasites, and then placed in media containing

575 MPA/xanthine 24 h later to select for restoration of HXGPRT. MPA/xanthine-resistant parasites
576 were cloned by limiting dilution into a 96 well plate. Wells containing single plaques were picked
577 7 days later and expanded. Genomic DNA was extracted from clones using a Proteinase K
578 treatment detailed elsewhere (85). Successful tagging of TgLaforin was verified using
579 sequencing, immunoblotting, and IFA.

580 *ME49ΔHXΔTgLaforin* ("ΔTgLaf"): TgLaforin was disrupted using a CRISPR-Cas9 mediated
581 strategy as detailed above, with several differences. Briefly, a single sgRNA was designed to
582 target the first exon of TgLaforin with the top hit from EuPaGDT (**Table S1**). To disrupt
583 TgLaforin with a selectable drug marker, DHFR-TS*, a pyrimethamine-resistant mutant of the
584 DHFR gene, containing a 5'-NcGra7 promotor and DHFR 3'UTR was amplified from pJET-
585 NcGra7_DHFR (**Table S2**). Amplification utilized primers containing 40 nt extensions
586 homologous to the 5'- and 3'-UTR of TgLaforin to encourage homologous recombination-
587 mediated whole-gene replacement with the drug cassette (**Table S3**). Both the PCR-amplified
588 DHFR* homology cassette and the CRISPR-Cas-GFP plasmid were transfected and FACS-
589 sorted as described above. GFP+ parasites underwent drug selection in pyrimethamine.
590 Parasites were then cloned and expanded as detailed above. Successful integration of the
591 DHFR* cassette into the TgLaforin locus was verified using PCR with inside/out primer pairs
592 to the chimeric, interrupted gene (**Table S3**). Loss of TgLaforin transcription was verified by
593 purifying RNA from TgLaforin clones on RNeasy spin columns (Qiagen). Using the Promega
594 Reverse Transcriptase System, cDNA was synthesized from RNA extracts. Primers designed
595 for full-length TgLaforin amplification were then used to verify loss of TgLaforin cDNA in
596 knockout lines.

597 *ME49ΔHXΔTgLaforin+ChrVI-TgLaforin* ("COMP"): Complementation of TgLaforin was also
598 executed using a CRISPR-mediated strategy. A sgRNA to a neutral locus on chromosome VI

599 identified previously (55) was generated using the same mutagenesis strategy as above (**Table**
600 **S1 and S3**). A full length TgLaforin cDNA containing its endogenous 5'UTR (2000 bp upstream
601 from gDNA) was synthesized by GenScript and inserted into a pHA3x-LIC vector (**Table S2**)
602 containing a C-terminal HA tag and a DHFR 3'UTR, linked to the HXGPRT selectable marker
603 (named "TgLaforin-HA3x-LIC"; also used above for endogenous tagging to create the
604 TgLaforin-HA line). The entire construct (5'UTR:TgLaforin-cDNA:DHFR-3'UTR:HXGPRT) was
605 amplified from the vector and co-transfected into ΔTgLaf parasites with the CRISPR-Cas9
606 plasmid as done above. Successful transformants that received the HXGPRT marker were
607 selected with MPA/xanthine. Successful insertion of TgLaforin along with its promoter was
608 verified using PCR (**Table S3**), immunoblotting, and IFA with an anti-HA antibody (Abcam).
609
610 ***Immunofluorescence (IF) staining***
611 HFFs were grown on glass coverslips until confluent and subsequently infected. Infected HFFs
612 were fixed with either methanol (MeOH) (100%, -20ºC) or methanol-free paraformaldehyde
613 (PFA) (4% in phosphate-buffered saline (PBS); Electron Microscopy Sciences) as indicated
614 below for each antibody. Infected HFFs fixed with PFA were permeabilized in 0.1% TritonX-
615 100 in PBS++ (PBS containing 0.5 mM $CaCl_2$ and 0.5 mM $MgCl_2$) for 10 min at room
616 temperature (RT). Primary and secondary antibodies were diluted in 3% (w/v) bovine serum
617 albumin (BSA; Fisher) in PBS++. Samples were first incubated with the primary antibody (αHA-
618 1:1,000; αSAG-1:10,000; αGAP45-1:5,000; IV58B6-1:50) at RT for 45 min, washed 3x with
619 PBS++, and then incubated with fluorescent secondary antibodies (1:2,000) and 4',6-
620 diamidino-2-phenylindole (DAPI; 300 nM) for 45 min. Secondary antibodies (Invitrogen) were
621 conjugated to either Oregon Green or Texas Red fluorophores and specific to the species and

622 class of primary antibody used. Samples were then washed 3x with PBS++ before mounting
623 the coverslip on a glass slide using MOWIOL mounting media.
624 IF staining was visualized using a Zeiss AxioVision upright microscope with a 100X 1.4
625 numerical-aperture oil immersion objective, and images were acquired using a grayscale Zeiss
626 AxioCam MRM digital camera. Grayscale images were pseudo-colored in ImageJ using
627 magenta (Texas Red), yellow (Oregon Green), and cyan (DAPI), and further alterations to
628 brightness and contrast were also made in ImageJ when deemed appropriate. For all assays
629 in which staining intensity was compared across treatments and parasite lines, concentrations
630 of antibodies, exposure times, and alterations to brightness/contrast were identical.
631 Colocalization of fluorescent antibodies/reagents was quantified using Pearson's coefficient
632 calculated with the JACoP plugin on ImageJ (86).
633
634 ***PAS staining***
635 PAS staining was done on infected HFFs fixed in 4% PFA and permeabilized as above.
636 Coverslips were then washed 3x in tap water before the addition of 1% periodic acid (Sigma-
637 Aldrich) for 5 min. Coverslips were then washed with three changes of tap water. Schiff's
638 reagent (diluted 1:4 in tap water) was added for 15 min. Coverslips were subsequently washed
639 10x with tap water to develop stain before being incubated with DAPI for 10 min and then
640 mounted as above. PAS-stained samples were visualized using fluorescence microscopy
641 (excitation: 545 nm, emission: 605 nm). When PAS was co-stained with antibodies, primary
642 antibodies were incubated with PAS-stained slides overnight in BSA at 4 $^{o}$C before standard
643 secondary staining.
644 Samples treated with acid-$\alpha$-amyloglucosidase (GAA) (from *Aspergillus niger*, >260 U/mL,
645 Sigma) were incubated with GAA after permeabilization. GAA was diluted 1:50 in 50 mM

646 sodium phthalate buffer, pH 5.5, and samples were treated for 24 h at room temperature.
647 Untreated controls were incubated in phthalate buffer without GAA. Samples were then stained
648 with PAS or IV58B6 as described in the IF-staining workflow above.
649
650 ***In vitro bradyzoite conversion assay***
651 Tachyzoites were converted to bradyzoites *in vitro* using alkaline stress as has been done
652 previously with several modifications (87). HFFs grown were infected with tachyzoites in
653 standard cell culture media. 4 h later, media was replaced with RPMI 1640 (Gibco 31800022)
654 supplemented with 50 mM HEPES and adjusted to pH 8.2 with NaOH. Parasites were then
655 cultured for 2-6 days at 37$^{o}$C, ambient $CO_2$, and sealed in Parafilm. Media was replaced every
656 other day to maintain the basic pH. Parasites were fixed in PFA and stained with fluorescein
657 conjugated *Dolichos biflorus* agglutinin (DBA; 1:1000, Vector Laboratories) and PAS. Images
658 were obtained in grayscale on a Zeiss AxioVision upright microscope as described above.
659 To determine the degree of labeling with DBA or PAS, the Fiji/ImageJ (88) was used to create
660 a binary mask outlining cysts that was applied to the PAS-stained image to measure the
661 greyscale intensity of each ROI (i.e. each individual vacuole/*in vitro* cyst).
662
663 ***Transmission electron microscopy of in vitro tachyzoites and bradyzoites***
664 Transmission-electron microscopy (TEM) was performed as done previously (89). Blocks were
665 stained at the University of Kentucky's Imaging Center in the College of Arts and Sciences.
666 Blocks were trimmed and sectioned on an ultramicrotome with a diamond knife. Sections were
667 placed on copper grids and then contrast stained with lead citrate. Micrographs were collected
668 at the University of Kentucky's Electron Microscopy Center on a Talos F200X TEM (Thermo)
669 operated at 200 kV accelerating voltage with a 50 μm objective aperture inserted to enhance

670 contrast using a 16M pixel 4k x 4k CMOS camera (Ceta, Thermo Scientific). AG size and
671 grayscale values were measured in ImageJ.
672
673 ***Immunoblotting***
674 Parasites were syringe lysed from host cells, pelleted, and $2x10^6$ parasites were resuspended
675 in SDS-PAGE sample buffer and boiled for 10 min before being run on a single lane of a 10%
676 polyacrylamide gel. The gel was then transferred to a 0.2 μm PVDF membrane (BioRad) using
677 a Turbotransfer System (BioRad) for 7 min at 25 V. The PVDF membrane was blocked in 5%
678 (w/v) non-fat milk in Tris-buffered saline plus Tween-20 detergent (TBST; 0.1% Tween-20) for
679 20 min before being probed with a primary antibody (αHA-1:1,000; αGAP45-1:5,000; αSRS9-
680 1:1,000; αSAG1-1:10,000) in non-fat milk overnight at 4ºC (Cell Signaling C29F4). The blot
681 was washed 3x with TBST before probing with either HRP-conjugated α-rabbit or α-mouse-
682 IgG (Jackson Laboratories). Blot was washed and developed for 5 min using SuperSignal™
683 West Pico PLUS (Thermo Scientific) and visualized on a GelDoc station (BioRad).
684
685 ***Steady state polar metabolite analysis***
686 Parasites were prepared as previously described (60). Confluent HFFs were infected with
687 parasites at a multiplicity of infection (MOI) of 2 to achieve a high density of parasites after 48
688 h of growth (>80% cells containing >32 parasites each). Plates containing infected HFFs were
689 placed on ice, media removed, and the monolayer was washed 2X with ice-cold PBS.
690 Parasites were harvested on ice in a 4 ºC cold-room. Cells were scraped from plate surface,
691 resuspended in PBS (8 plates/50 mL PBS), and centrifuged at 1000*g* for 10 min at 4 ºC. PBS
692 was removed, the cell pellet was resuspended in 2 mL PBS, and syringe passaged
693 successively in 23 G and 27 G needles. The soluble host cell lysate was removed by

694 centrifugation (1000*g*). The pellet was resuspended in 5 mL PBS and host-cell debris was
695 removed by syringe-filtering the suspension through a 3 μm filter (Whatman). Filtered parasites
696 were then pelleted, resuspended in 1 mL PBS, and counted on a hemacytometer. Parasites
697 were pelleted a final time at 14,000*g* for 30 s at 4 °C, supernatant was removed, and pelleted
698 parasites were flash frozen in liquid nitrogen and stored at -80 °C until metabolite extraction.
699 *Polar metabolite extraction:* Polar metabolites were extracted in 0.5 mL -20 °C 50% methanol
700 (MeOH) containing 20 μM L-norvaline (procedural control) for 30 min on ice. During the 30 min
701 incubation, samples were regularly vortexed. Samples were then centrifuged at 14000*g* for 10
702 min to pellet insoluble material (protein, DNA, RNA, and glycans). Supernatant containing polar
703 metabolites and pellet were dried separately on a SpeedVac (Thermo) at $10^{-3}$ mBar until
704 methanol (MeOH) was completely sublimated and only dried pellet remained.
705 *Pellet hydrolysis and extraction:* Dried fraction containing protein was hydrolyzed by
706 resuspending the pellet in 2 N HCl (final concentration) at 95°C for 2 h. Hydrolysis was
707 quenched, and hydrolyzed amino acids were extracted by the addition of an equal volume of
708 100% MeOH with 40 μM L-norvaline such that the final concentration was 50% and 20 μM,
709 respectively. Extraction and drying then proceeded as described above.
710 *Sample derivatization*: Dried samples (both polar metabolites and hydrolyzed protein) were
711 derivatized in 70 μL 20 mg/mL methoxyamine hydrochloride in pyridine for 90 min at 30 °C.
712 Samples were then centrifuged at 14000*g* for 10 min to remove any particulate, and 50 μL of
713 the methoxyamine supernatant was mixed with 80 μL *N*-methyl-*N*-trimethylsilyl
714 trifluoroacetamide (MSTFA) and incubated for 30 min at 37°C. Samples were then transferred
715 to amber glass chromatography vials and analyzed by GC/MS.
716

717 *GC/MS analysis*: Metabolites were analyzed on an Agilent 7800B GC coupled to a 5977B MS
718 detector using a previously established protocol (90). Automated Mass Spectral Deconvolution
719 and Identification System (AMDIS) was used to analyze metabolites by matching metabolites
720 to the FiehnLib metabolomics library via retention time and fragmentation pattern.
721 Quantification of metabolite levels was performed in Mnova. Sample abundance was
722 normalized to L-norvaline (procedural control) and protein from the protein pellet (experimental
723 control). Steady state metabolites are presented as the mean of three independent replicates.
724

725 ***Conventional plaque assays***

726 HFFs were grown in 12-well plates until confluent. HFFs were subsequently infected with 200
727 parasites/well under standard cell culture conditions. Wells were washed with PBS to remove
728 residual invasion media, and media was changed to glutamine replete or depleted media 4 h
729 post-infection to allow for invasion. Plates remained undisturbed for 10 days before the infected
730 HFFs were fixed with 100%, -20$^{o}$C MeOH for 20 min, stained with 1% crystal violet solution for
731 20 min, and then the plaques were de-stained with repeated tap water washes. Zones of lysis
732 (white clearings) could be visualized against intact cells (purple). Images of plaques were
733 obtained by scanning plates on an Epson Perfection V600 photo scanner at a resolution of 600
734 dpi. The plaques were measured by pixel area using ImageJ. Plaque assays were conducted
735 on three independent replicates, and plaque size from these experiments were aggregated to
736 highlight variability in plaque sizes.
737

738 ***Egress assays***

739 HFFs were grown to confluency in 35 mm glass bottom dishes (MatTek, P35G-0-14-C). Two
740 days before infecting HFFs on glass bottom dishes, both HFFs and parasites were

741 independently pre-treated in either glutamine-replete or -depleted media (see above for media
742 formulations). After 48 h pre-treatment, $10^5$ parasites of each line (WT, ΔTgLaf, and COMP) in
743 each pre-treatment (gln+/-) were added to fresh dishes and allowed to grow for 48 h so that
744 most vacuoles contained >32 parasites each. Several hours before egress, media in each
745 infected plate was adjusted to 1.5 mL and allowed to equilibrate at 37°C in 5% $CO_2$. The
746 calcium ionophore A23187 (Cayman Chemical Company) was prepared as a 2 mM stock in
747 DMSO and diluted in (+/-) gln media to make a 4X concentration of 12 μM and maintained at
748 37°C throughout the assay. Zaprinast was likewise prepared as a 100 mM stock in DMSO and
749 diluted into media at a 4X concentration of 2 mM. Egress was triggered by the addition of 0.5
750 mL 4X A23187 to infected HFFs (3.0 μM final concentration) or 0.5 mL 4X-zaprinast (500 μM
751 final concentration). Egress was monitored on a Nikon Eclipse Ti2 inverted microscope with a
752 40X phase air objective modified with a 1.5X optivar. Several fields containing vacuoles were
753 selected from each plate, and an image was obtained 10 s after triggering egress from each
754 field once every 5 s for 5 mins (61 images/field) on a Nikon DS-Ri2 color camera. Videos of
755 each field were assembled on NIS Elements software. Egress was monitored using standard
756 deviation of pixel intensity and determined by inflection point of change in standard deviation
757 of pixel intensity. Inflection point was calculated by fitting a gaussian curve to the first derivative
758 of the standard deviation in pixel intensity and calculating the mean of the curve. Technical
759 replicates (fields on each plate) were averaged for each biological replicate (average of fields
760 from each plate).
761
762 ***Replication assays***
763 HFFs were grown on glass coverslips in a 24-well plate until confluent. Two days before
764 infecting HFFs on coverslips, both HFFs and parasites were independently pre-treated in either

765 glutamine-replete or -depleted media. After pre-treatment, $10^4$ parasites of each line (WT,
766 ΔTgLaf, and COMP) in each condition (gln+/-) were added to 3 coverslips each. 24 hours later,
767 infected HFFs were fixed in MeOH and stained with Rb-α-SAG1 (1:10,000) and DAPI for ease
768 of visualization. Counting of parasites/vacuole was performed for each line/condition on coded
769 blinded slides with the identity of samples revealed upon completion of the counting. A total of
770 three independent replicates were performed.
771
772 ***Modified plaque assays***
773 A modified plaque assay was developed to visualize foci of infection at higher magnification
774 where zones of clearing were not readily evident. Confluent HFF monolayers on glass
775 coverslips in 24 well plates were infected with WT, ΔTgLaf, and COMP parasites in replete
776 media for 4 hours to allow for invasion. The monolayers were washed gently 3 times with PBS
777 and either fresh replete media or glutamine-depleted media were added for 3 or 6 days to
778 appropriate wells. Infected monolayers were washed and fixed with MeOH (-20 $^{o}$C) and
779 subjected to IF using DAPI and GRA3, an antibody that detects the PVM. Individual plaques
780 were imaged on coded blinded slides using a 10X objective, and their perimeters and
781 encompassed areas were measured using Image J. Host cell clearance within plaques was
782 similarly measured, and the extent of clearance was represented as a percentage for each
783 individual plaque. A total of three independent replicates were performed.
784
785 ***Mouse infection***
786 4- to 6-week old CBA/J mice of both sexes (Jackson Laboratories, Bar Harbor, ME) were
787 injected intraperitoneally (i.p.) with either 100 WT, ΔTgLaf, or COMP tachyzoites, or with 20
788 tissue-cysts from brain homogenates derived from previously infected mice. In either case,

789 parasites/cysts were suspended in a final volume of 0.2 mL serum-free, Opti-MEM media
790 (Gibco). Mice were then monitored and assigned a body index score daily. Monitoring
791 frequency increased to twice a day once symptomatic throughout the course of infection as
792 previously described (68). When symptomatic, mice were administered a gel diet and wet chow
793 on the cage floor and given 0.25-0.5 mL saline solution subcutaneously as needed. Moribund
794 mice were humanely euthanized. Euthanasia of both moribund mice and mice sacrificed at the
795 time of tissue cyst harvest was performed by $CO_2$ asphyxiation, followed by cervical
796 dislocation. The number of mice used for each experiment is indicated within relevant figures.
797 All protocols were carried out under the approval of the University of Kentucky's Institutional
798 Animal Care and Use Committee (IACUC).
799
800 ***Tissue cyst purification***
801 Tissue cysts were purified as previously described using discontinuous Percoll gradients (7,
802 91). Processing of two sex/infection-matched brains was performed on each gradient. Cysts
803 were collected in 1 mL fractions from the bottom of the centrifuged Percoll gradient using a
804 peristaltic pump adjusted to a flow rate of 2 mL/min. To quantify tissue cysts, 10-20 μL of each
805 fraction was placed into 100 μL PBS in the well of a 96-well plate, pelleted and directly
806 enumerated at 20X magnification in each well. Total cysts per mouse were calculated by
807 summing the total number of cysts in each fraction and dividing the total by two to adjust for
808 brain homogenization in pairs. Each pair of mice was presented as a single averaged data
809 point. Tissue cysts were pelleted onto slides using a Cytospin centrifuge and fixed and stored
810 in 100% MeOH (-20$^{o}$C) until staining.
811
812

813 ***Determination of cyst diameter and packing density***

814 Tissue cysts fixed on slides were co-stained with DAPI and DBA to obtain nuclear profiles for
815 bradyzoites and an outline of the cyst for diameter measurement. The diameter was
816 determined in Fiji (ImageJ) by drawing a circle around the cyst and computing the diameter.
817 Packing density was determined as described previously (7). Briefly, DAPI images of cysts
818 were opened in BradyCount1.0, and threshold levels were adjusted as needed to capture all
819 nuclear profiles. After BradyCount1.0 provided the number of bradyzoite nuclei, the packing
820 density was determined by dividing the number of bradyzoites by the volume of the section.
821 The formula describing this calculation is: $\mathbf{PD = N / (\pi r^2 \, x \, h)}$ where PD=packing density, N = #
822 of bradyzoites, r = radius calculated from cyst diameter, and h = height of section (0.238 μm).
823 At least 10 cysts from each line at each timepoint were measured.

824

825 ***Preparation of in vivo tissue cysts for TEM imaging***

826 To prepare *T. gondii* tissue cysts generated *in vivo* for TEM, cysts were isolated from the
827 brains of infected mice as detailed above through the counting step. The Percoll fraction
828 containing mouse red blood cells (RBCs) was also recovered. After combining Percoll
829 fractions containing tissue cysts and diluting with PBS to a volume of 15 mL (maximum of two
830 1-mL fractions were combined before dilution), cysts were pelleted for 15 min at 1000*g* at 4
831 $^{o}$C. To maximize cyst recovery, 10 mL supernatant was removed, and the remaining 5 mL was
832 divided into 1 mL fractions for the top 4 mL, and the bottom 1 mL directly above the pellet was
833 sub-fractionated into 100 μL volumes. Typically, the majority of cysts were localized to within
834 300 μL of the Percoll pellet, rather than in the pellet itself. Sub-fractions containing cysts were
835 once again combined and diluted (typically 200-300 μL diluted with 1-mL PBS) in a 1.5 mL
836 Eppendorf tube, and then pelleted in a swinging-bucket rotor for 10 min at 1000*g* and 4 $^{o}$C.

837 Leaving the pellet undisturbed, all but 50 μL of the supernatant was removed. A small volume
838 (~5-10 μL) of the reserved RBC fraction was added to the remaining volume for ease of
839 visualizing the pellet throughout the remaining processing steps.
840 To ensure the detection of the relatively rare cyst population, a previously described protocol
841 (71, 72) was adapted to concentrate the cysts into a small agarose block. A 1.33X fixative
842 solution of glutaraldhehyde (GA) in cacodylate buffer was prepared containing 4% GA and 133
843 mM sodium cacodylate. 150 μL fixative solution was then added to the 50 μL sample, bringing
844 the total volume to 200 μL such that the final concentration of GA was 3% and sodium
845 cacodylate was 100 mM. Cysts were then incubated at room temperature for 1 h in fixative.
846 While cysts were in fixative, 4% low-melt agarose (BioRad) was prepared in 100 mM sodium
847 cacodylate buffer and kept liquid at 70 $^{o}$C until needed. After fixation, cysts were pelleted again
848 at 1000*g* for 10 min at room temperature in a table-top centrifuge. All but 50 μL supernatant
849 was once again removed, and 200 μL warm low-melt agarose was slowly added on top of
850 fixed, pelleted cysts (3.2% agarose, final concentration). Suspension was then centrifuged
851 again at 1000*g* for 10 min at 30 $^{o}$C to keep the agarose semi-liquid, and then placed on ice for
852 20 min to solidify agarose. After solidification, entire agarose plug was removed from tube with
853 a small a wooden dowel that had been whittled into a thin scoop. This agarose plug was placed
854 in a Petri dish, and the pellet was carefully cut out of the plug with a razor blade to create a 1
855 $mm^3$ block. The agarose block was then stored in 1X GA/cacodylate buffer overnight at 4$^{o}$C.
856 Processing of the block from post-stain onward was then identical to TEM processing
857 described above. During sectioning, thick sections cut on a glass knife were stained with
858 toluidine blue and examined for cysts using a light microscope prior to ultra-thin sectioning
859 once the cyst containing later was identified.
860

861 ***Data analyses***

862 All data analyses, including graph preparation and statistics, were performed using GraphPad
863 Prism 9.

864 ----------

865 ***Acknowledgements:*** The authors wish to acknowledge Dr. Elizabeth Watts who conducted
866 early exploratory studies that encouraged the pursuit of this project, Jim Begley (Imaging
867 Center, University of Kentucky) for preparation of EM samples and willingness to explore new
868 methodologies for isolating rare *in vivo* cysts, Jillian Cramer (Electron Microscopy Center,
869 University of Kentucky) for acquisition of TEM images, and Jennifer Strange (Flow Cytometry
870 and Immune Monitoring Core Facility, University of Kentucky) for assistance with isolation of
871 GFP+ *T. gondii* mutants using flow cytometry.

872

873 ***Author contributions:***

874 Conceptualization (R.D.M., A.P.S., M.S.G.), Methodology (R.D.M., A.D., C.O.B., A.P.S.,
875 M.S.G.), Formal analysis (R.D.M., C.A.T., J.S.M., L.E.A.Y., R.C.S., C.W.V.K., A.P.S.),
876 Investigation (R.D.M., C.A.T., J.S.M., L.E.A.Y., A.P.S.), Resources (M.S.G., A.P.S.), Writing—
877 original draft (R.D.M.), Writing—review and editing (all authors), Visualization (R.D.M., C.A.T.,
878 J.S.M., A.P.S.), Supervision (M.S.G., A.P.S.), Project administration (R.D.M., M.S.G., A.P.S.),
879 Funding acquisition (R.D.M., C.W.V.K., M.S.G., A.P.S.).

880

881 ***Funding:*** This work was supported by: GRFP 1247392 to R.D.M., NIH grants R21 AI150631
882 and R01 AI145335 to A.P.S., and NIH grants R35 NS116824, P01 NS097197, and NSF CHE
883 1808304 to C.W.V.K. and MCB 2308488 to M.S.G.

884

885 ***Conflicts of Interest:*** none

886

887 ***Abbreviations:*** AG, amylopectin granule; CDPK2, calcium dependent protein kinase2;
888 COMP, TgLaforin-complemented parasite line; CRISPR, clustered regularly interspersed short
889 palindromic repeats; DBA, *Dolichos biflorus* agglutinin lectin; ΔTgLaf, TgLaforin-KO parasite
890 line; DHFR, dihydrofolate reductase; FACS, fluorescence activated cell sorting; GAA, acid-α-
891 amyloglucosidase; Gal-NAc, N-acetylgalactosamine; GAPDH1, glyceraldehyde-3-phosphate
892 dehydrogenase; GC/MS, gas chromatography/mass spectrometry; GFP, green fluorescent
893 protein; GT1, glucose transporter1; GWD, glucan, water di-kinase; HA, hemagglutinin; HFF,
894 human foreskin fibroblasts; HK, hexokinase; HR, homologous recombination; HXGPRT,
895 hypoxanthine-xanthine-guanine phosphoribosyl transferase; IF, immunofluorescence; i.p.,
896 intraperitoneally; KO, knockout; MPA, mycophenolic acid; PAM, protospacer adjacent motif;
897 PAS, periodic acid-Schiff; PV, parasitophorous vacuole; PWD, phospho-glucan, water di-
898 kinase; PYK1, pyruvate kinase1; RBC, red blood cell; RT, room temperature; SEX4, starch-
899 excess4; SS, starch/glycogen synthase; TCA, tricarboxylic acid; TEM, transmission electron
900 microscopy; UTR, untranslated region; WT, parental ME49ΔHXGPRT parasite line used in this
901 study.

902

903

904 **REFERENCES**

905

906 1. Flegr J, Prandota J, Sovičková M, Israili ZH. Toxoplasmosis--a global threat. Correlation of
907 latent toxoplasmosis with specific disease burden in a set of 88 countries. PLoS One.
908 2014;9(3):e90203.

909 2. Jones JL, Dubey JP. Foodborne toxoplasmosis. Clinical infectious diseases : an official
910 publication of the Infectious Diseases Society of America. 2012;55(6):845-51.

911 3. Derouin F, Garin YJF. *Toxoplasma gondii* : Blood and tissue kinetics during acute and
912 chronic infections in mice. Experimental Parasitology. 1991;73(4):460-8.

913 4. Jeffers V, Tampaki Z, Kim K, Sullivan WJ, Jr. A latent ability to persist: differentiation in
914 *Toxoplasma gondii* . Cell Mol Life Sci. 2018;75(13):2355-73.

915 5. Luft BJ, Remington JS. Toxoplasmic Encephalitis in AIDS. Clinical Infectious Diseases.
916 1992;15(2):211-22.

917 6. Cerutti A, Blanchard N, Besteiro S. The Bradyzoite: A Key Developmental Stage for the
918 Persistence and Pathogenesis of Toxoplasmosis. Pathogens. 2020;9(3):234.

919 7. Watts E, Zhao Y, Dhara A, Eller B, Patwardhan A, Sinai AP. Novel approaches reveal that
920 *Toxoplasma gondii* bradyzoites within tissue cysts are dynamic and replicating entities in vivo.
921 MBio. 2015;6(5):e01155-15.

922 8. Place BC, Troublefield C, Murphy RD, Sinai AP, Patwardhan A. Computer Aided Image
923 Processing to Facilitate Determination of Congruence in Manual Classification of Mitochondrial
924 Morphologies in *Toxoplasma gondii* Tissue Cysts. Annu Int Conf IEEE Eng Med Biol Soc.
925 2021;2021:3509-13.

926 9. MacNeill GJ, Mehrpouyan S, Minow MA, Patterson JA, Tetlow IJ, Emes MJ, et al. Starch
927 as a source, starch as a sink: the bifunctional role of starch in carbon allocation. Journal of
928 Experimental Botany. 2017;68(16):4433-53.
929 10. Dubey JP, Frenkel JK. Feline toxoplasmosis from acutely infected mice and the
930 development of Toxoplasma cysts. J Protozool. 1976;23(4):537-46.
931 11. Coppin A, Dzierszinski F, Legrand S, Mortuaire M, Ferguson D, Tomavo S.
932 Developmentally regulated biosynthesis of carbohydrate and storage polysaccharide during
933 differentiation and tissue cyst formation in *Toxoplasma gondii* . Biochimie. 2003;85(3-4):353-
934 61.
935 12. Coppin A, Varre J-S, Lienard L, Dauvillee D, Guerardel Y, Soyer-Gobillard M-O, et al.
936 Evolution of plant-like crystalline storage polysaccharide in the protozoan parasite *Toxoplasma*
937 *gondii* argues for a red alga ancestry. Journal of Molecular Evolution. 2005;60(2):257-67.
938 13. Guérardel Y, Leleu D, Coppin A, Liénard L, Slomianny C, Strecker G, et al. Amylopectin
939 biogenesis and characterization in the protozoan parasite *Toxoplasma gondii* , the intracellular
940 development of which is restricted in the HepG2 cell line. Microbes and infection. 2005;7(1):41-
941 8.
942 14. Uboldi AD, McCoy JM, Blume M, Gerlic M, Ferguson DJ, Dagley LF, et al. Regulation of
943 starch stores by a Ca2+-dependent protein kinase is essential for viable cyst development in
944 *Toxoplasma gondii* . Cell Host & Microbe. 2015;18(6):670-81.
945 15. Yang J, Yang C, Qian J, Li F, Zhao J, Fang R. *Toxoplasma gondii* α-amylase deletion
946 mutant is a promising vaccine against acute and chronic toxoplasmosis. Microb Biotechnol.
947 2020.

948 16. Yang J, He Z, Chen C, Zhao J, Fang R. Starch branching enzyme 1 is important for
949 amylopectin synthesis and cyst reactivation in *Toxoplasma gondii* . Microbiology Spectrum.
950 2022;10(3):e01891-21.
951 17. Lyu C, Yang X, Yang J, Hou L, Zhou Y, Zhao J, et al. Role of amylopectin synthesis in
952 *Toxoplasma gondii* and its implication in vaccine development against toxoplasmosis. Open
953 Biol. 2021;11(6):200384.
954 18. Blume M, Nitzsche R, Sternberg U, Gerlic M, Masters SL, Gupta N, et al. A *Toxoplasma*
955 *gondii* gluconeogenic enzyme contributes to robust central carbon metabolism and is essential
956 for replication and virulence. Cell host & microbe. 2015;18(2):210-20.
957 19. Ralton JE, Sernee MF, McConville MJ. Evolution and function of carbohydrate reserve
958 biosynthesis in parasitic protists. Trends Parasitol. 2021.
959 20. Sernee MF, Ralton JE, Nero TL, Sobala LF, Kloehn J, Vieira-Lara MA, et al. A family of
960 dual-activity glycosyltransferase-phosphorylases mediates mannogen turnover and virulence
961 in Leishmania parasites. Cell host & microbe. 2019;26(3):385-99. e9.
962 21. Kötting O, Kossmann J, Zeeman SC, Lloyd JR. Regulation of starch metabolism: the age
963 of enlightenment? Curr Opin Plant Biol. 2010;13(3):321-9.
964 22. Silver DM, Kötting O, Moorhead GB. Phosphoglucan phosphatase function sheds light on
965 starch degradation. Trends in plant science. 2014;19(7):471-8.
966 23. Stitt M, Zeeman SC. Starch turnover: pathways, regulation and role in growth. Curr Opin
967 Plant Biol. 2012;15(3):282-92.
968 24. Ritte G, Lloyd JR, Eckermann N, Rottmann A, Kossmann J, Steup M. The starch-related
969 R1 protein is an alpha -glucan, water dikinase. Proc Natl Acad Sci U S A. 2002;99(10):7166-
970 71.

971 25. Kötting O, Pusch K, Tiessen A, Geigenberger P, Steup M, Ritte G. Identification of a novel
972 enzyme required for starch metabolism in Arabidopsis leaves. The phosphoglucan, water
973 dikinase. Plant Physiol. 2005;137(1):242-52.
974 26. Takeda Y, Hizukuri S. Re-examination of the action of sweet-potato beta-amylase on
975 phosphorylated (1→4)-χ-d-glucan. Carbohydrate Research. 1981;89(1):174-8.
976 27. Edner C, Li J, Albrecht T, Mahlow S, Hejazi M, Hussain H, et al. Glucan, water dikinase
977 activity stimulates breakdown of starch granules by plastidial beta-amylases. Plant Physiol.
978 2007;145(1):17-28.
979 28. Hejazi M, Fettke J, Haebel S, Edner C, Paris O, Frohberg C, et al. Glucan, water dikinase
980 phosphorylates crystalline maltodextrins and thereby initiates solubilization. Plant J.
981 2008;55(2):323-34.
982 29. Hansen PI, Spraul M, Dvortsak P, Larsen FH, Blennow A, Motawia MS, et al. Starch
983 phosphorylation--maltosidic restrains upon 3'- and 6'-phosphorylation investigated by chemical
984 synthesis, molecular dynamics and NMR spectroscopy. Biopolymers. 2009;91(3):179-93.
985 30. Murphy RD, Chen T, Lin J, He R, Wu L, Pearson CR, et al. The Toxoplasma glucan
986 phosphatase TgLaforin utilizes a distinct functional mechanism that can be exploited by
987 therapeutic inhibitors. Journal of Biological Chemistry. 2022:102089.
988 31. Kloehn J, Krishnan A, Tonkin CJ, McConville MJ, Soldati-Favre D. Chapter 10 - Metabolic
989 networks and metabolomics. In: Weiss LM, Kim K, editors. *Toxoplasma gondii* (Third Edition):
990 Academic Press; 2020. p. 451-97.
991 32. Chen P, Lyu C, Wang Y, Pan M, Lin X, Shen B. Key roles of amylopectin synthesis and
992 degradation enzymes in the establishment and reactivation of chronic toxoplasmosis. Animal
993 Diseases. 2023;3(1):1-11.

994 33. Zeeman SC, Northrop F, Smith AM, Rees T. A starch-accumulating mutant of Arabidopsis
995 thaliana deficient in a chloroplastic starch-hydrolysing enzyme. Plant J. 1998;15(3):357-65.
996 34. Kötting O, Santelia D, Edner C, Eicke S, Marthaler T, Gentry MS, et al. STARCH-EXCESS4
997 is a laforin-like Phosphoglucan phosphatase required for starch degradation in Arabidopsis
998 thaliana. Plant Cell. 2009;21(1):334-46.
999 35. Lafora GR. Band 205. In: Johannes O, editor. XXI Über das Vorkommen amyloider
1000 Körperchen im Innern der Ganglienzellen; zugleich Ein Beitrag zum Studium der amyloiden
1001 Substanz im Nervensystem: De Gruyter; 2021. p. 295-303.
1002 36. Minassian BA, Lee JR, Herbrick JA, Huizenga J, Soder S, Mungall AJ, et al. Mutations in a
1003 gene encoding a novel protein tyrosine phosphatase cause progressive myoclonus epilepsy.
1004 Nat Genet. 1998;20(2):171-4.
1005 37. Gentry MS, Guinovart JJ, Minassian BA, Roach PJ, Serratosa JM. Lafora disease offers a
1006 unique window into neuronal glycogen metabolism. Journal of Biological Chemistry.
1007 2018;293(19):7117-25.
1008 38. Duran J, Hervera A, Markussen KH, Varea O, López-Soldado I, Sun RC, et al. Astrocytic
1009 glycogen accumulation drives the pathophysiology of neurodegeneration in Lafora disease.
1010 Brain. 2021;144(8):2349-60.
1011 39. Sugi T, Tu V, Ma Y, Tomita T, Weiss LM. *Toxoplasma gondii* requires glycogen
1012 phosphorylase for balancing amylopectin storage and for efficient production of brain cysts.
1013 MBio. 2017;8(4):e01289-17.
1014 40. Cao XZ, Wang JL, Elsheikha HM, Li TT, Sun LX, Liang QL, et al. Characterization of the
1015 role of Amylo-alpha-1, 6-glucosidase protein in the infectivity of *Toxoplasma gondii* . Frontiers
1016 in Cellular and Infection Microbiology. 2019;9:418.

1017 41. Wang J-L, Li T-T, Elsheikha HM, Liang Q-L, Zhang Z-W, Wang M, et al. The protein
1018 phosphatase 2A holoenzyme is a key regulator of starch metabolism and bradyzoite
1019 differentiation in *Toxoplasma gondii* . Nature communications. 2022;13(1):7560.
1020 42. Zhao M, Yang Y, Shi Y, Chen X, Yang Y, Pan L, et al. PP2Acα-B′/PR61 Holoenzyme of
1021 *Toxoplasma gondii* Is Required for the Amylopectin Metabolism and Proliferation of
1022 Tachyzoites. Microbiology Spectrum. 2023;11(3):e00104-23.
1023 43. Gentry MS, Dowen RH, Worby CA, Mattoo S, Ecker JR, Dixon JE. The phosphatase laforin
1024 crosses evolutionary boundaries and links carbohydrate metabolism to neuronal disease. The
1025 Journal of cell biology. 2007;178(3):477-88.
1026 44. Gentry MS, Pace RM. Conservation of the glucan phosphatase laforin is linked to rates of
1027 molecular evolution and the glucan metabolism of the organism. BMC evolutionary biology.
1028 2009;9(1):138.
1029 45. Baba O. Production of monoclonal antibody that recognizes glycogen and its application
1030 for immunohistochemistry. Kokubyo Gakkai zasshi The Journal of the Stomatological Society,
1031 Japan. 1993;60(2):264-87.
1032 46. Oe Y, Baba O, Ashida H, Nakamura KC, Hirase H. Glycogen distribution in the microwave-
1033 fixed mouse brain reveals heterogeneous astrocytic patterns. Glia. 2016;64(9):1532-45.
1034 47. van de Weerd R, Berbís MA, Sparrius M, Maaskant JJ, Boot M, Paauw NJ, et al. A Murine
1035 Monoclonal Antibody to Glycogen: Characterization of Epitope-Fine Specificity by Saturation
1036 Transfer Difference (STD) NMR Spectroscopy and Its Use in Mycobacterial Capsular α-Glucan
1037 Research. Chembiochem. 2015;16(6):977-89.
1038 48. Skurat AV, Segvich DM, DePaoli-Roach AA, Roach PJ. Novel method for detection of
1039 glycogen in cells. Glycobiology. 2017;27(5):416-24.

1040 49. Guimarães EV, de Carvalho L, Barbosa HS. An alternative technique to reveal
1041 polysaccharides in *Toxoplasma gondii* tissue cysts. Mem Inst Oswaldo Cruz. 2003;98(7):915-
1042 7.
1043 50. Sidik SM, Hackett CG, Tran F, Westwood NJ, Lourido S. Efficient genome engineering of
1044 *Toxoplasma gondii* using CRISPR/Cas9. PloS one. 2014;9(6):e100450.
1045 51. Fritz HM, Buchholz KR, Chen X, Durbin-Johnson B, Rocke DM, Conrad PA, et al.
1046 Transcriptomic analysis of toxoplasma development reveals many novel functions and
1047 structures specific to sporozoites and oocysts. PloS one. 2012;7(2):e29998.
1048 52. Choi CP, Moon AS, Back PS, Jami-Alahmadi Y, Vashisht AA, Wohlschlegel JA, et al. A
1049 photoactivatable crosslinking system reveals protein interactions in the *Toxoplasma gondii*
1050 inner membrane complex. PLoS biology. 2019;17(10):e3000475.
1051 53. Shen B, Brown KM, Lee TD, Sibley LD. Efficient gene disruption in diverse strains of
1052 *Toxoplasma gondii* using CRISPR/CAS9. mBio. 2014;5(3):e01114-14.
1053 54. Sidik SM, Huet D, Ganesan SM, Huynh MH, Wang T, Nasamu AS, et al. A Genome-wide
1054 CRISPR Screen in Toxoplasma Identifies Essential Apicomplexan Genes. Cell.
1055 2016;166(6):1423-35.e12.
1056 55. Markus BM, Bell GW, Lorenzi HA, Lourido S. Optimizing systems for Cas9 expression in
1057 *Toxoplasma gondii* . MSphere. 2019;4(3):e00386-19.
1058 56. Yang J, Yang C, Qian J, Li F, Zhao J, Fang R. *Toxoplasma gondii* α-amylase deletion
1059 mutant is a promising vaccine against acute and chronic toxoplasmosis. Microb Biotechnol.
1060 2020;13(6):2057-69.
1061 57. Xia N, Ye S, Liang X, Chen P, Zhou Y, Fang R, et al. Pyruvate homeostasis as a
1062 determinant of parasite growth and metabolic plasticity in *Toxoplasma gondii* . MBio.
1063 2019;10(3):e00898-19.

1064 58. Brewer MK, Uittenbogaard A, Austin GL, Segvich DM, DePaoli-Roach A, Roach PJ, et al.
1065 Targeting pathogenic Lafora bodies in Lafora disease using an antibody-enzyme fusion. Cell
1066 metabolism. 2019;30(4):689-705. e6.
1067 59. Sun RC, Young LEA, Bruntz RC, Markussen KH, Zhou Z, Conroy LR, et al. Brain glycogen
1068 serves as a critical glucosamine cache required for protein glycosylation. Cell Metab.
1069 2021;33(7):1404-17 e9.
1070 60. King EF, Cobbold SA, Uboldi AD, Tonkin CJ, McConville MJ. Metabolomic Analysis of
1071 *Toxoplasma gondii* Tachyzoites. *Toxoplasma gondii* : Springer; 2020. p. 435-52.
1072 61. Nitzsche R, Zagoriy V, Lucius R, Gupta N. Metabolic cooperation of glucose and glutamine
1073 is essential for the lytic cycle of obligate intracellular parasite *Toxoplasma gondii* . Journal of
1074 Biological Chemistry. 2016;291(1):126-41.
1075 62. Oppenheim RD, Creek DJ, Macrae JI, Modrzynska KK, Pino P, Limenitakis J, et al.
1076 BCKDH: the missing link in apicomplexan mitochondrial metabolism is required for full
1077 virulence of *Toxoplasma gondii* and Plasmodium berghei. PLoS pathogens. 2014;10(7).
1078 63. Endo T, Sethi K, Piekarski G. *Toxoplasma gondii* : Calcium Ionophore A23187-mediated
1079 exit of trophozoites from infected murine macrophages. Experimental parasitology.
1080 1982;53(2):179-88.
1081 64. Lourido S, Tang K, Sibley LD. Distinct signalling pathways control Toxoplasma egress and
1082 host-cell invasion. The EMBO journal. 2012;31(24):4524-34.
1083 65. Ferguson DJ. Use of molecular and ultrastructural markers to evaluate stage conversion of
1084 *Toxoplasma gondii* in both the intermediate and definitive host. International journal for
1085 parasitology. 2004;34(3):347-60.

1086 66. Sinai AP. Chapter 11 - The *Toxoplasma gondii* Parasitophorous Vacuole Membrane: A
1087 Multifunctional Organelle in the Infected Cell. In: Weiss LM, Kim K, editors. *Toxoplasma gondii*
1088 (Second Edition). Boston: Academic Press; 2014. p. 375-87.
1089 67. Boothroyd JC, Black M, Bonnefoy S, Hehl A, Knoll LJ, Manger ID, et al. Genetic and
1090 biochemical analysis of development in *Toxoplasma gondii* . Philos Trans R Soc Lond B Biol
1091 Sci. 1997;352(1359):1347-54.
1092 68. Troublefield CA, Miracle JS, Murphy RD, Donkin RW, Sinai AP. Factors influencing tissue
1093 cyst yield in a murine model of chronic toxoplasmosis. Infection and Immunity. 2023:e00566-
1094 22.
1095 69. Watts EA, Dhara A, Sinai AP. Purification *Toxoplasma gondii* Tissue Cysts Using Percoll
1096 Gradients. Curr Protoc Microbiol. 2017;45:20C 2 1-C 2 19.
1097 70. Quach EV, Cao B, Babacarkhial E, Ho D, Sharma J, Guiton PS. Phosphoglucomutase 1
1098 contributes to optimal cyst development in *Toxoplasma gondii* . BMC Research Notes.
1099 2022;15(1):1-8.
1100 71. Kumar S, Ciraolo G, Hinge A, Filippi MD. An efficient and reproducible process for
1101 transmission electron microscopy (TEM) of rare cell populations. J Immunol Methods.
1102 2014;404:87-90.
1103 72. Kumar S, Filippi MD. An Alternative Approach for Sample Preparation with Low Cell
1104 Number for TEM Analysis. J Vis Exp. 2016(116).
1105 73. Sinai AP, Suvorova ES. The RESTRICTION checkpoint: a window of opportunity governing
1106 developmental transitions in *Toxoplasma gondii* . Current opinion in microbiology. 2020;58:99-
1107 105.

1108 74. Xue Y, Theisen TC, Rastogi S, Ferrel A, Quake SR, Boothroyd JC. A single-parasite
1109 transcriptional atlas of *Toxoplasma gondii* reveals novel control of antigen expression. Elife.
1110 2020;9:e54129.
1111 75. Olson WJ, Martorelli Di Genova B, Gallego-Lopez G, Dawson AR, Stevenson D, Amador-
1112 Noguez D, et al. Dual metabolomic profiling uncovers Toxoplasma manipulation of the host
1113 metabolome and the discovery of a novel parasite metabolic capability. PLoS pathogens.
1114 2020;16(4):e1008432.
1115 76. Zeeman SC, Smith SM, Smith AM. The diurnal metabolism of leaf starch. Biochemical
1116 Journal. 2007;401(1):13-28.
1117 77. Mahlow S, Orzechowski S, Fettke J. Starch phosphorylation: insights and perspectives.
1118 Cellular and molecular life sciences. 2016;73(14):2753-64.
1119 78. Niittyla T, Comparot-Moss S, Lue WL, Messerli G, Trevisan M, Seymour MD, et al. Similar
1120 protein phosphatases control starch metabolism in plants and glycogen metabolism in
1121 mammals. The Journal of biological chemistry. 2006;281(17):11815-8.
1122 79. Shukla A, Olszewski KL, Llinás M, Rommereim LM, Fox BA, Bzik DJ, et al. Glycolysis is
1123 important for optimal asexual growth and formation of mature tissue cysts by *Toxoplasma*
1124 *gondii* . International journal for parasitology. 2018;48(12):955-68.
1125 80. Blume M, Rodriguez-Contreras D, Landfear S, Fleige T, Soldati-Favre D, Lucius R, et al.
1126 Host-derived glucose and its transporter in the obligate intracellular pathogen *Toxoplasma*
1127 *gondii* are dispensable by glutaminolysis. Proceedings of the National Academy of Sciences.
1128 2009;106(31):12998-3003.
1129 81. Dubey R, Staker BL, Foe IT, Bogyo M, Myler PJ, Ngô HM, et al. Membrane skeletal
1130 association and post-translational allosteric regulation of *Toxoplasma gondii* GAPDH1. Mol
1131 Microbiol. 2017;103(4):618-34.

1132 82. Araujo FG, Huskinson-Mark J, Gutteridge WE, Remington JS. In vitro and in vivo activities
1133 of the hydroxynaphthoquinone 566C80 against the cyst form of *Toxoplasma gondii* .
1134 Antimicrobial agents and chemotherapy. 1992;36(2):326-30.
1135 83. Doggett JS, Nilsen A, Forquer I, Wegmann KW, Jones-Brando L, Yolken RH, et al.
1136 Endochin-like quinolones are highly efficacious against acute and latent experimental
1137 toxoplasmosis. Proc Natl Acad Sci U S A. 2012;109(39):15936-41.
1138 84. McPhillie MJ, Zhou Y, Hickman MR, Gordon JA, Weber CR, Li Q, et al. Potent
1139 Tetrahydroquinolone Eliminates Apicomplexan Parasites. Front Cell Infect Microbiol.
1140 2020;10:203.
1141 85. Brown KM, Long S, Sibley LD. Conditional Knockdown of Proteins Using Auxin-inducible
1142 Degron (AID) Fusions in *Toxoplasma gondii* . Bio Protoc. 2018;8(4).
1143 86. Bolte S, Cordelières FP. A guided tour into subcellular colocalization analysis in light
1144 microscopy. J Microsc. 2006;224(Pt 3):213-32.
1145 87. Mayoral J, Di Cristina M, Carruthers VB, Weiss LM. *Toxoplasma gondii* : Bradyzoite
1146 Differentiation In Vitro and In Vivo. Methods in molecular biology. 2020;2071:269-82.
1147 88. Schindelin J, Arganda-Carreras I, Frise E, Kaynig V, Longair M, Pietzsch T, et al. Fiji: an
1148 open-source platform for biological-image analysis. Nat Methods. 2012;9(7):676-82.
1149 89. Sinai AP, Webster P, Joiner KA. Association of host cell endoplasmic reticulum and
1150 mitochondria with the *Toxoplasma gondii* parasitophorous vacuole membrane: a high affinity
1151 interaction. J Cell Sci. 1997;110 ( Pt 17):2117-28.
1152 90. Andres DA, Young LEA, Veeranki S, Hawkinson TR, Levitan BM, He D, et al. Improved
1153 workflow for mass spectrometry–based metabolomics analysis of the heart. Journal of
1154 Biological Chemistry. 2020;295(9):2676-86.

1155 91. Watts EA, Dhara A, Sinai AP. Purification *Toxoplasma gondii* Tissue Cysts Using Percoll
1156 Gradients. Curr Protoc Microbiol. 2017;45:20c.2.1-c.2.19.
1157
1158

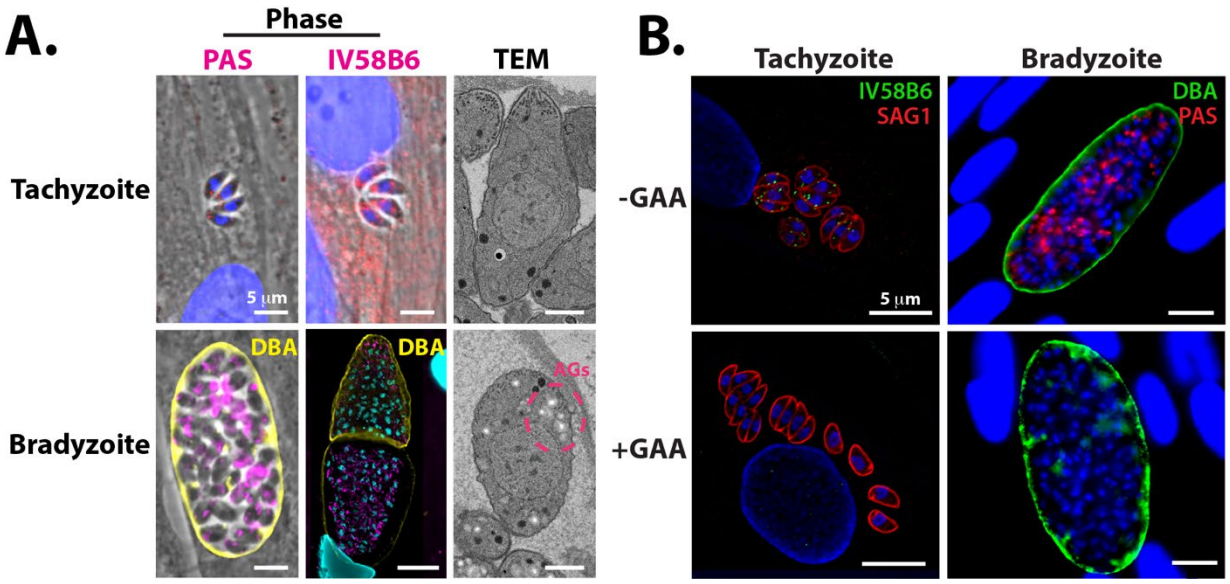


**Figure 1.** Glucan dynamics in *T. gondii* ME49 tachyzoites and bradyzoites. **A,** Microscopy-based glucan evaluation of *T. gondii* tachyzoites and bradyzoites using PAS (left), IV58B6 (middle; α-glycogen IgM mAb), and TEM (right). **B,** GAA digest of AGs in tachyzoites and bradyzoites confirms specificity of IV58B6 antibody and PAS staining. All scale bars = 5 µm.

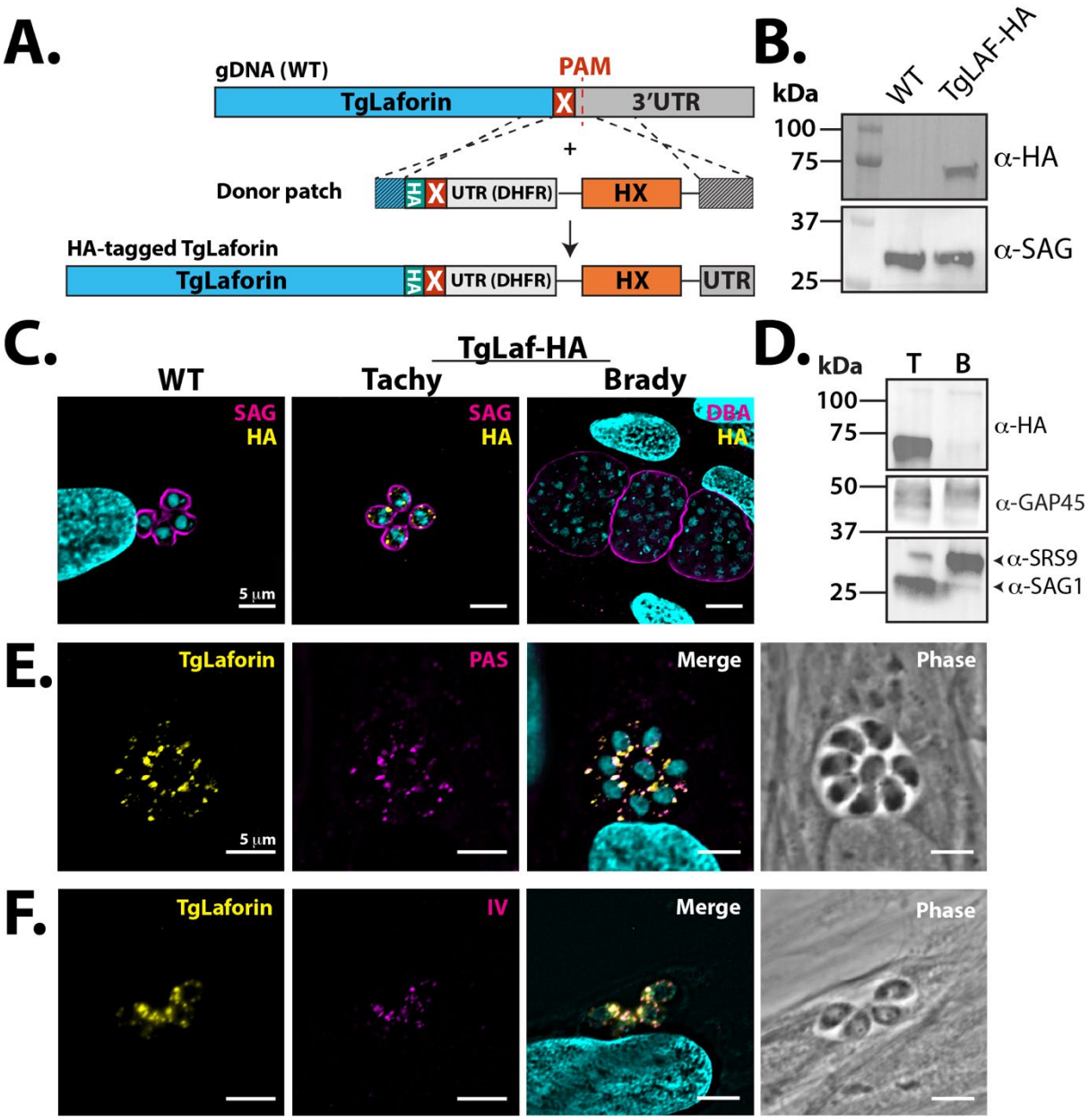


**Figure 2.** Endogenous tagging and localization of TgLaforin. **A,** Schematic depicting the TgLaforin 3xHA-epitope tagging strategy. X = stop codon. **B,** Successful tagging of TgLaforin (62 kDa) was verified using immunoblot analysis with an α-HA antibody with SAG1 used as a loading control. **C,** IFA in WT/tagged parasites with α-HA antibody. **D,** Western blot analysis of TgLaforin expression levels in tachyzoites (T) and bradyzoites (B). GAP45 is the loading control. Decrease in SAG1 alongside increase in SRS9 confirms tachyzoite to bradyzoite conversion. **E**, IFA of TgLaforin colocalization with PAS. Pearson's coefficient: 0.765. **F**, IFA of TgLaforin colocalization with IV58B6. Pearson's coefficient: 0.737. All scale bars = 5 μm.

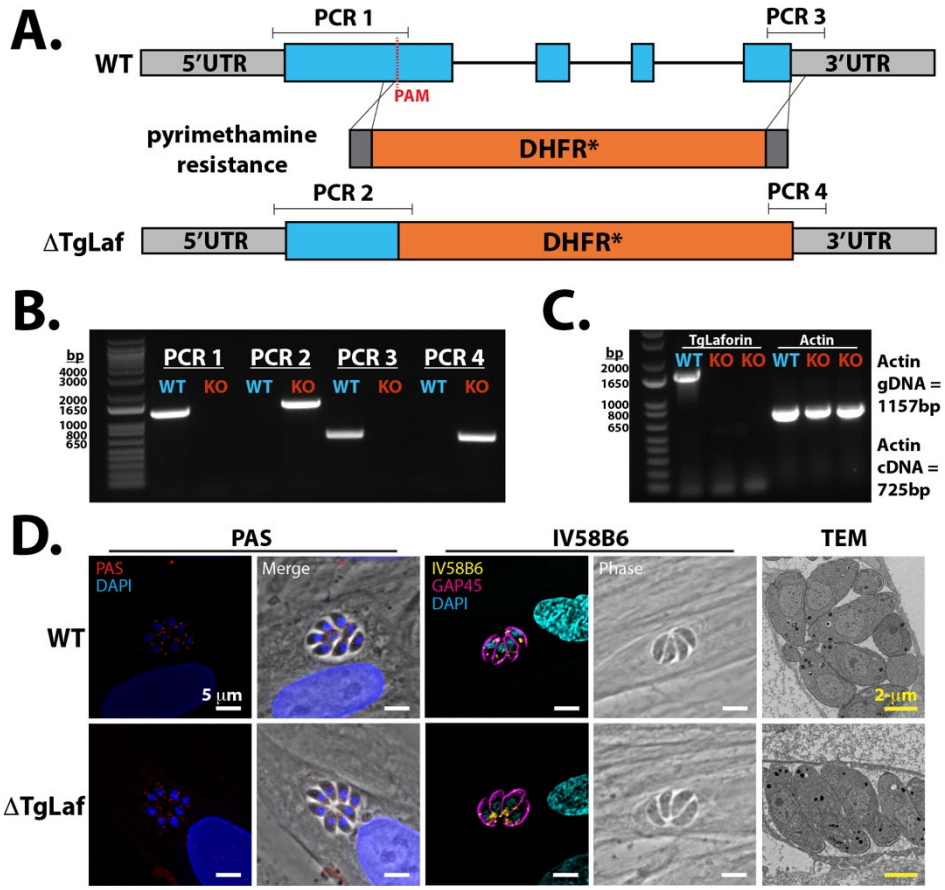


**Figure 3.** Loss of TgLaforin results in no gross glucan abnormalities under glucose replete conditions. **A,** Schematic of TgLaforin KO strategy: the pyrimethamine-resistant DHFR* gene containing 40-nt homologous arms (dark gray boxes on either end of gene) was inserted into the TgLaforin locus via homologous recombination. A double stranded break was induced using CRISPR/Cas9-GFP with a PAM site in the first exon. **B,** Inside/out PCR verification of DHFR integration into the TgLaforin locus. Amplicons (PCR1-4) are illustrated in (A). **C,** Loss of TgLaforin mRNA was confirmed by amplifying full-length TgLaforin cDNA generated from both WT and ΔTgLaf strains. Actin cDNA amplification serves both as a loading control and as a control to verify the absence of gDNA. **D,** Analysis of glucan levels in ΔTgLaf tachyzoites using three different approaches: PAS and IV58B6 immunofluorescence staining, and TEM.

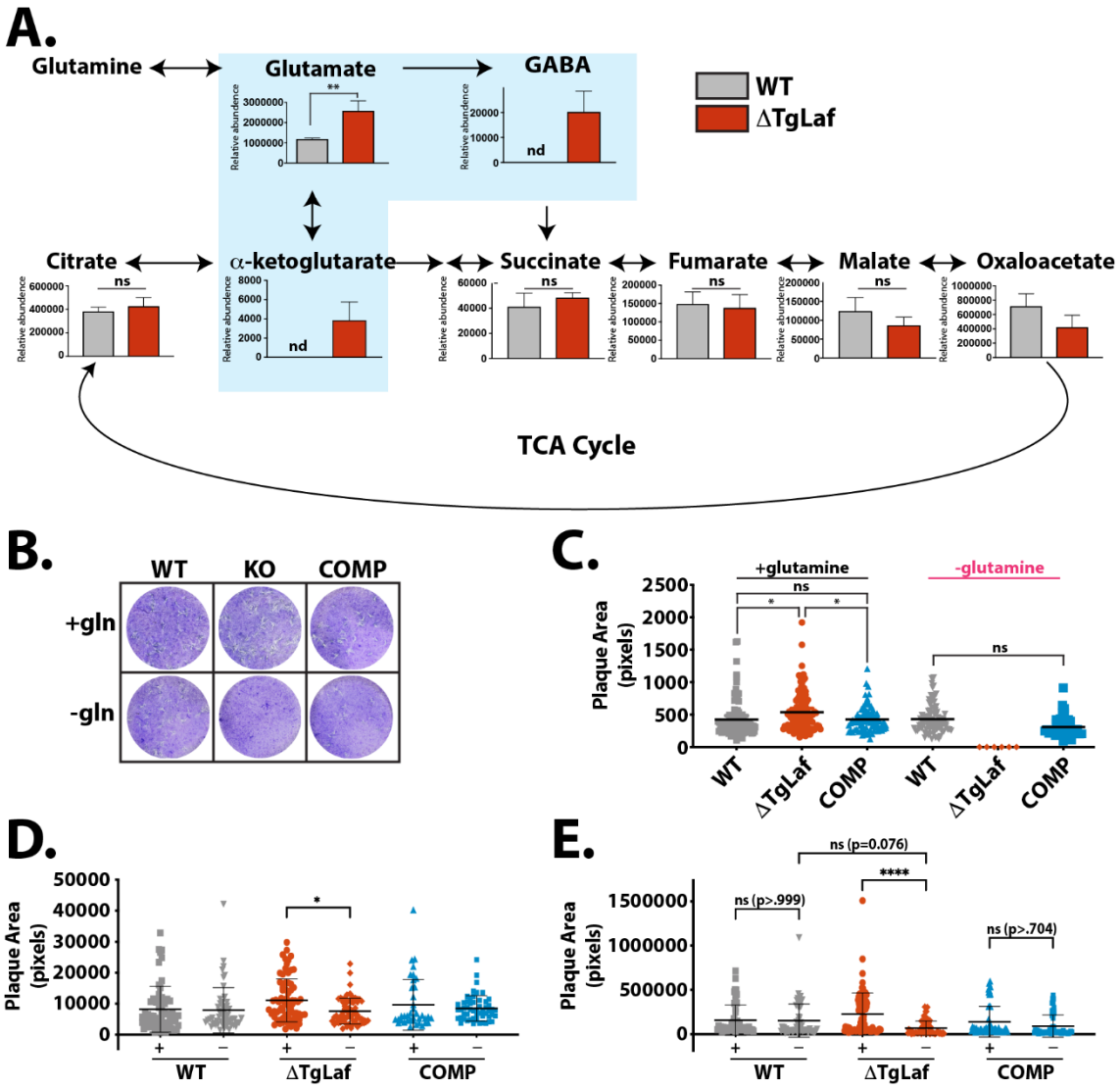


**Figure 4.** ΔTgLaf parasites are dependent on glutamine for normal plaque formation. **A**, Steady-state metabolomics suggests upregulation of glutaminolysis in ΔTgLaf parasites. Metabolite levels of intracellular tachyzoites were analyzed after 48 hours of growth in HFFs by GC/MS analysis. Data were collected from 3 independent replicates. Statistical comparisons were done using unpaired two-tailed t-tests. Statistical significance is as follows: **p<0.01, ns=p>0.05, nd=not detected. **B**, Representative plaque assays are presented for each line and condition. **C**, Total plaque area (pixels) was measured across three independent replicates. **D**, Pixel area of nascent plaques after 3 days of growth as monitored by IF microscopy under both glutamine replete (+) and depleted conditions (-). **E**, Pixel area of plaques monitored as in (D) after 6 days of growth. Statistical comparisons for C-E were done using an ordinary one-way ANOVA using Tukey's post-hoc test to correct for multiple comparisons. Statistical significance is indicated as follows: *p<0.05, ****p<0.0001, ns=p>0.05.

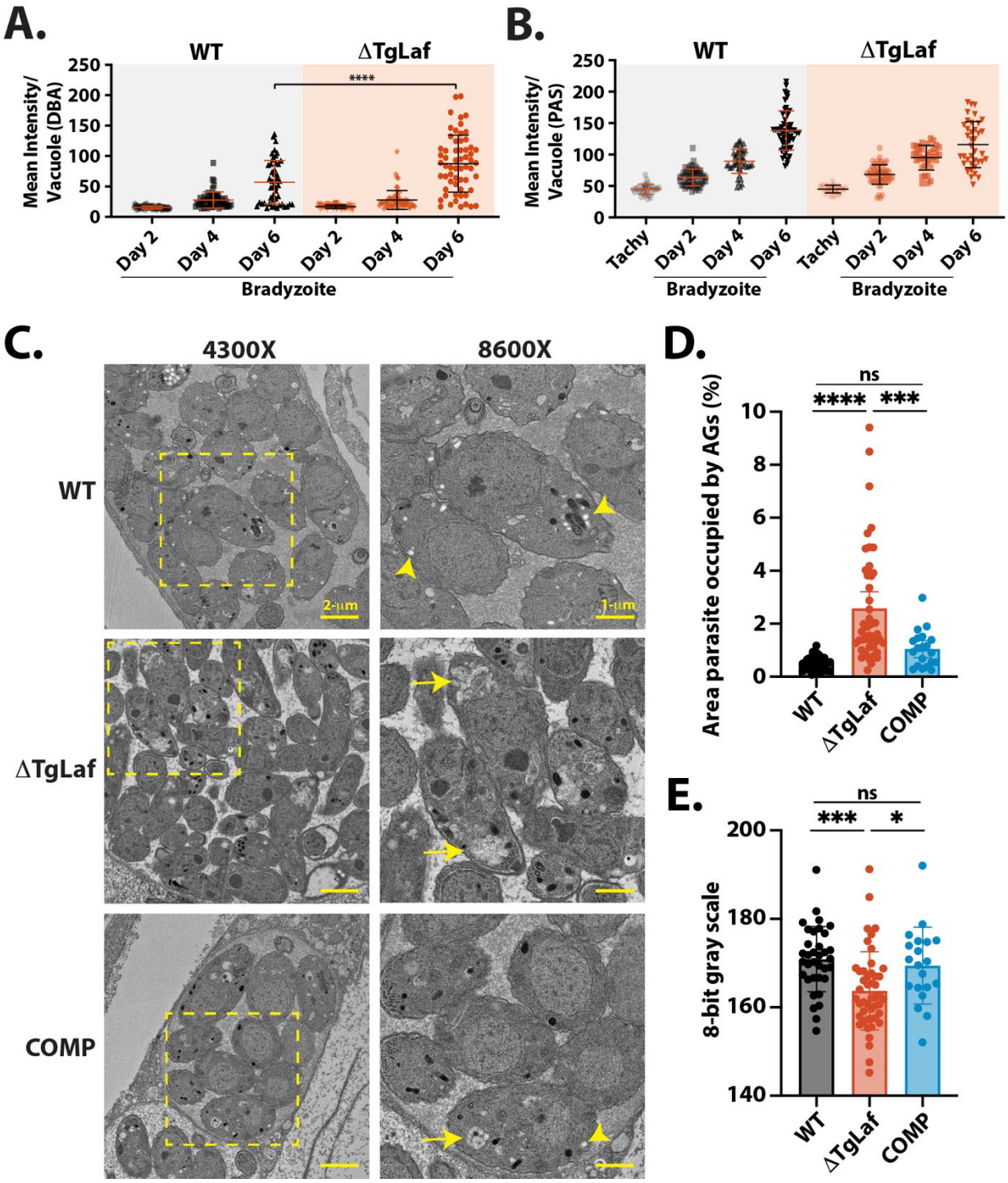


**Figure 5**. Loss of TgLaforin results in aberrant glucan morphology and accumulation in *in vitro* bradyzoites only visible by TEM. **A,** *In vitro* tachyzoite to bradyzoite conversion efficiency of ΔTgLaf vs WT parasites as measured by DBA intensity. **B,** Change in PAS levels during bradyzoite conversion by PAS levels. **C,** Representative TEM images of bradyzoites from each indicated parasite line. At 4300x magnification, scale bar = 2 µm; at 8600x magnification, scale bar = 1 µm. Arrowhead = canonical AG (white, round/ovoid); Arrow = aberrant AG (grey, flattened, multi-lobed). **D,** Quantification of relative parasite AG content and **E,** AG grayness

across parasite lines using 8-bit grayscale (0=black, 255=white). Statistical comparisons were done using an ordinary one-way ANOVA with Tukey's post-hoc test to correct for multiple comparisons. Statistical significance is indicated as follows: *$p<0.05$, ***$p<0.001$, ****$p<0.0001$, ns=$p>0.05$.

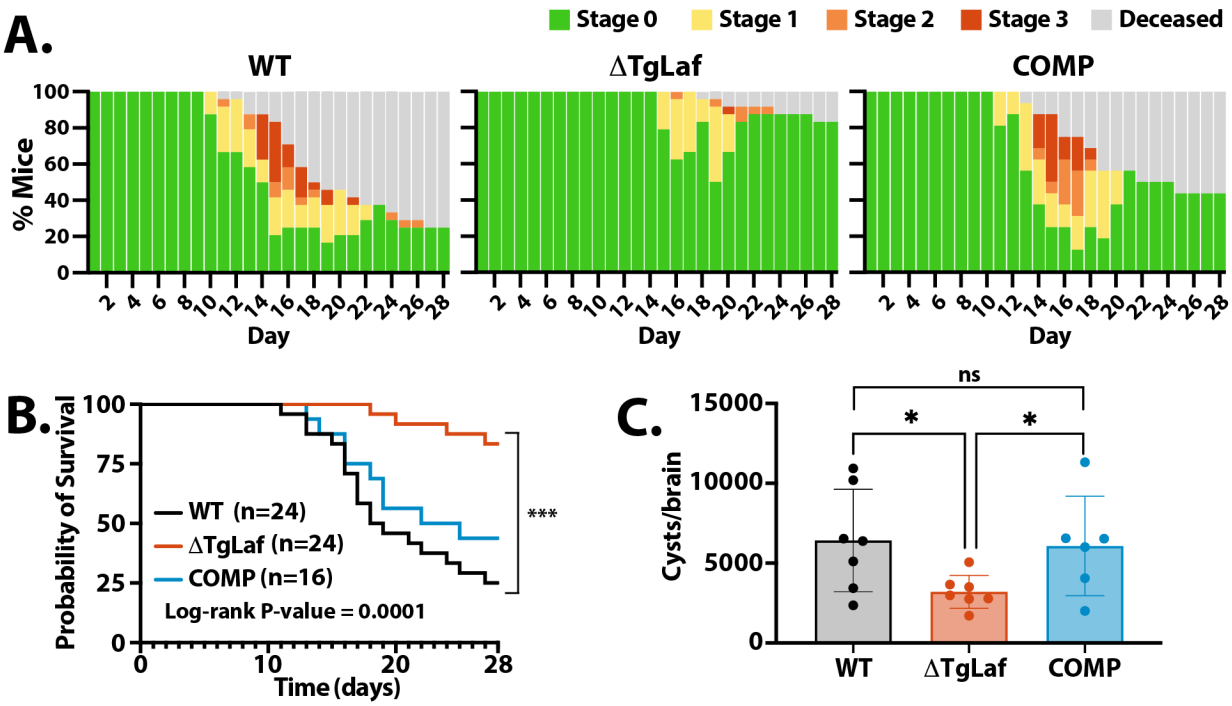


**Figure 6.** Loss of TgLaforin attenuates tachyzoite virulence and cyst burden in mice. Equal numbers of male and female CBA/J mice were infected i.p. with 100 tachyzoites from each group for monitoring symptoms and death: **A,** Symptomology throughout the acute phase of infection. Mice were monitored 1-2x/day and assigned a body score index ranging from asymptomatic (Stage 0) to moribund/deceased. **B,** Kaplan-Meier curve of mouse survival throughout acute tachyzoite infection. **C,** Mice that survived 4-weeks were euthanized, and cysts were counted as done previously (1, 2). Error bars depict SD from the mean. Statistical comparison for Kaplan Meier curves is indicated on plot, and statistical comparison of cyst burden was done using unpaired two-tailed t-tests. Statistical significance: *$p<0.05$, ***$p<0.0002$.

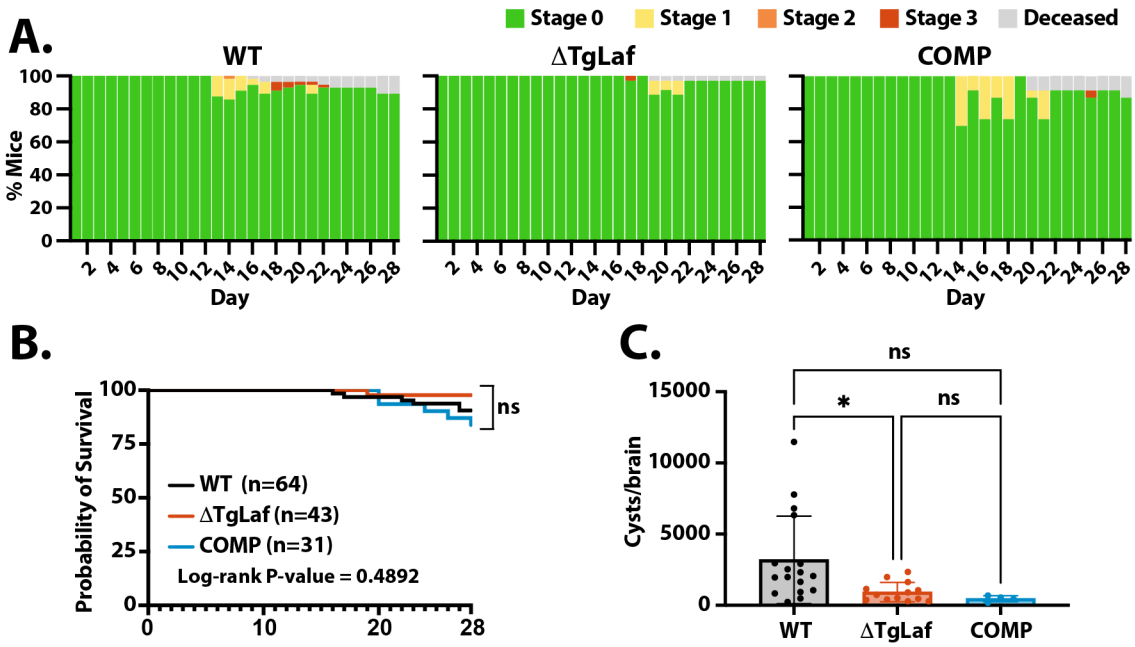


**Figure 7.** Mouse infection with ΔTgLaf tissue cysts results in milder illness and lower cyst burden. CBA/J mice were infected i.p. with 20 cysts taken from previously infected mouse brains and monitored for symptomology and death. **A,** Symptomology throughout the acute phase of infection as described in Figure 6B. **B,** Kaplan-Meier curve of mouse survival during acute tachyzoite infection. **C,** Cysts/brain after 4-week bradyzoite infection. Cyst numbers were determined as described in Figure 6C. Statistical comparison of cyst burden was done using unpaired two-tailed t-tests. Statistical significance: *p<0.05, ns=p>0.05.

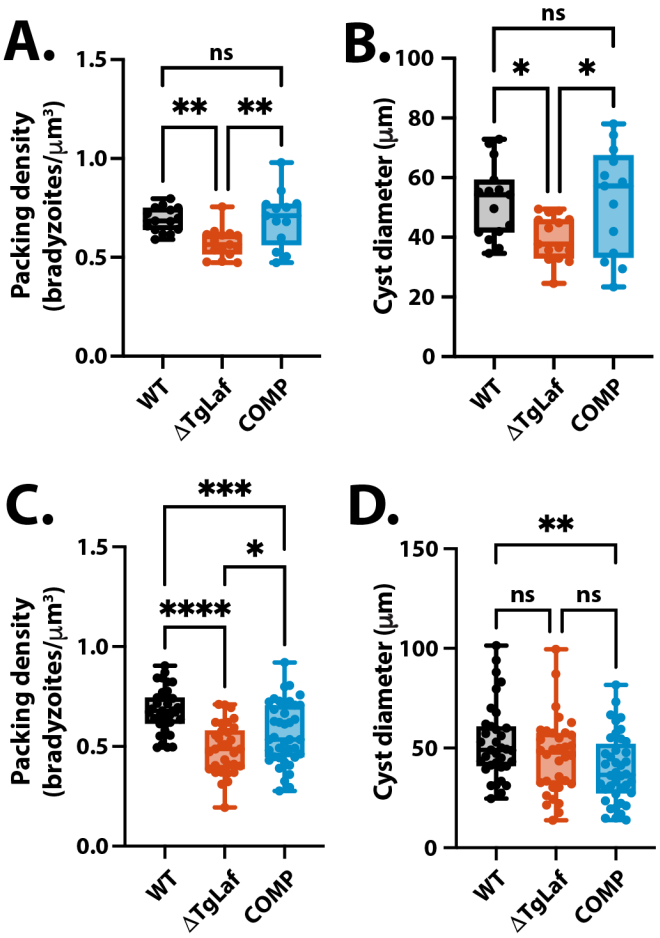


**Figure 8.** Cysts formed by ΔTgLaf parasites are smaller and less densely packed with bradyzoites. **A,** Packing density comparison among WT, ΔTgLaf, and COMP lines at week 4. Calculations were done using BradyCount1.0 to identify and quantify nuclear profiles from DAPI-stained tissue cysts (1). **B,** Cyst diameter comparison among WT, ΔTgLaf, and COMP lines as measured in ImageJ at week 4. **C,** Packing density comparison at week 6, as described in (A). **D,** Cyst diameter comparison at week 6, as described in (B). Statistical comparisons were done using an ordinary one-way ANOVA using Tukey's post-hoc test to correct for multiple comparisons. Error bars depict SD from the mean. Statistical significance is indicated as follows: *p<0.05, **p<0.01, ns=p>0.05.

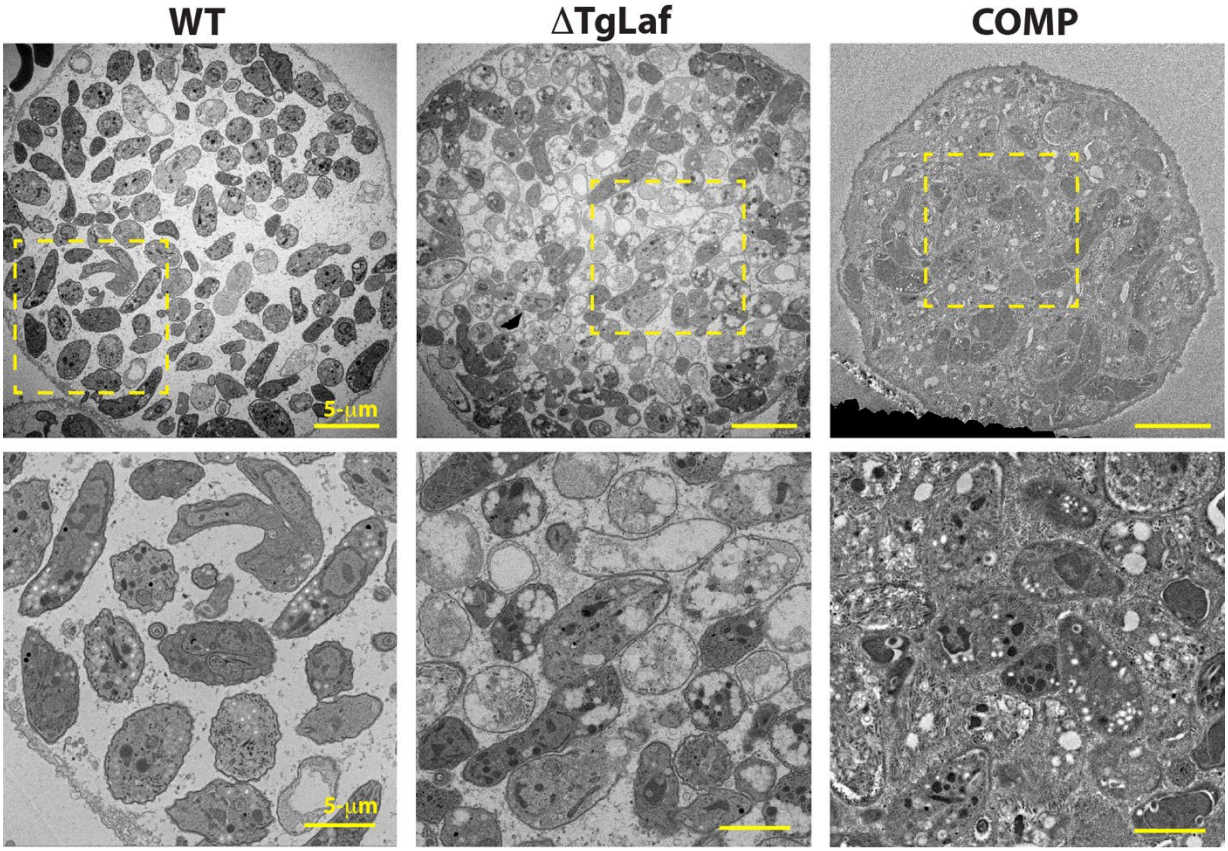


**Figure 9.** *T. gondii* bradyzoites accumulate excess AGs in the absence of TgLaforin. Upper panels: scale bar = 5 μm; lower panels (zoom of boxed region from upper panel): scale bar = 2 μm.